論文 / 著書情報
Article / Book Information

Title	Modeling and visualization of carrier motion in organic films by optical second harmonic generation and Maxwell-displacement current
Authors	Mitsumasa Iwamoto, Takaaki Manaka, Dai Taguchi
Citation	Journal of Physics D: Applied Physics, 48, , 373001/1-20
Pub. date	2015, 1
Note	このファイルは著者（最終）版です。 This file is author (final) version.
Note	This is an author-created, un-copyedited version of an article accepted for publication/published in Journal of Physics D: Applied Physics. IOP Publishing Ltd is not responsible for any errors or omissions in this version of the manuscript or any version derived from it. The Version of Record is available online at http://dx.doi.org/10.1088/0022-3727/48/37/373001.

Outline Topical review: J. Phys. D Applied Physics

Modeling and Visualization of Carrier Motion in Organic Films by Optical Second Harmonic Generation and Maxwell-Displacement Current

Mitsumasa Iwamoto, Takaaki Manaka, Dai Taguchi

Department of Physical Electronics, Tokyo Institute of Technology,
2-12-1 O-okayama, Meguro-ku, Tokyo 152-8552, Japan
Email: iwamoto@pe.titech.ac.jp

ABSTRACT

Probing and modeling of carrier motions in materials as well as in electronic devices is a fundamental research subject in science and electronics. According to the Maxwell electromagnetic field theory, carriers are a source of *electric field*. Therefore, by probing dielectric polarization caused by the electric field arising from moving carriers and dipoles, we can find a way to visualize the carrier motions in materials and in devices. The techniques used here are an electrical Maxwell-displacement current (MDC) measurement and a novel optical method based on electric field induced optical second harmonic generation (EFISHG) measurement. The MDC measurement probes changes of induced charge on electrodes, while the EFISHG probes nonlinear polarization induced in organic active layers due to coupling of electron clouds of molecules and electro-magnetic waves of incident laser beam in the presence of *dc* field caused from electrons and holes. Both measurements allow us to probe dynamical carrier motions in solids through detection of dielectric polarization phenomena originated from dipolar motions and electron transport. In this Topical review, on the basis of the Maxwell's electro-magnetism theory in 1873, which stems from the Faraday's idea, the concept for probing electron and hole transport in solids by using the EFISHG is discussed in comparison with the conventional time of flight (TOF) measurement. We then visualize carrier transit in organic devices, i.e., organic field effect transistors, organic light emitting diodes, organic solar cells, and others. We also show that visualizing EFISHG microscopic image is a novel way for characterizing the anisotropic carrier transport in organic thin films. We also discuss the concept of the detection of rotational dipolar motions in monolayers by means of the MDC measurement, which is capable of probing the change of dielectric spontaneous polarization formed by dipoles in organic monolayers. Finally we conclude that ideas and experiments on EFISHG and MDC lead to a novel way for analyzing dynamical motions of electrons, holes, and dipoles in solids, thus these are available in organic electronic device application.

1. Introduction

Probing and modeling of carrier transport in materials is a fundamental research subject in electronics and materials science. According to the Maxwell electromagnetic field theory [1,2], the total current flowing across solids is the sum of the conduction current and Maxwell displacement current (MDC). The conduction current flows when electrons and holes are conveyed under the external electric field formed by applied potentials on electrodes, and it flows steadily. Accordingly, we measure current-voltage (I-V) characteristics to study the carrier transport mechanism [3, 4]. In contrast, the MDC is generated when the electric flux density originating from electrons, holes, and dipoles changes with time, and it is basically a transient current and it flows whilst the electric flux density changes with time. Consequently, we can study dynamical motions of electrons and holes, and orientational dipolar motions in solids by probing the MDC [5,6]. In other words, on the basis of dielectric physics approach we can study dynamical carrier motion in solids. Generally, we measure transient currents that are generated by external stimuli, such as pulse voltage, light illumination, and heating. For example, thermally stimulated current measurement (TSC) is employed for studying dipolar depolarization in solids which are sandwiched between two electrodes, where a short circuit current is measured during heating [7-9]. What we measure by the TSC measurement is the change of the amount of induced charges on the electrodes due to disordering of aligned dipoles. Thus the recorded short circuit MDC traces the dynamical dipolar motion. This TSC technique is very simple, and we can use the concept of TSC measurement for studying dipolar motion in thin films, including organic monolayers on the order of nano-meters in thickness [9,10]. Technically, it is very difficult to prepare MIM devices with monolayers sandwiched between two electrodes. However, this technical problem does not matter, because we do not need to contact the monolayers with electrodes for detecting polarization of monolayers by the MDC measurement. Actually, to probe dynamical dipolar motion in monolayers on the water surface, a suspended electrode connected to a short circuit is used to measure the MDC [10-12]. That is, the change of the amount of charges induced on the suspended electrode above the monolayer is measured during the course of monolayer compression. Noteworthy that the change of induced charges on the suspended electrode will also appear due to the structural change of monolayer films such as phase transition and photo-isomerization, etc. [13-15]. In this Topical review, we will briefly discuss the principle of the MDC measurement and show the detection of Maxwell's current generated from organic monolayers.

In order to probe electron and hole transits across solids sandwiched between two electrodes, time-of-flight (TOF) technique is utilized [3-5,9,16,17]. What we measure by using this TOF technique is the change of amount of induced charge on the electrode connected to an

ammeter. Hence, the principle of the TOF measurement is basically the same as that of the MDC measurement used for studying monolayers associated with dipolar motion. In the conventional laser-TOF measurement [3,4,17], long-range carrier motion in solids is recorded as a transient current, from which we determine the transit time of carriers and then calculate the carrier mobility. This technique is very popular, and well used for the determination of the carrier mobility. However, there is a drawback in the measurement. For example, the location of carriers traveling across solid materials cannot be determined directly from the transient current recorded. The conventional laser-TOF measurement forces an elaborate mathematical approach on us for analyzing the traveling carriers, and this analysis leads to a puzzling situation in which there are many possible mathematical solutions to reproduce observed transient currents. This means that it is quite a task to trace actual carrier behavior in solids by the laser-TOF method. Furthermore, it is difficult to distinguish the carrier species, i.e., electrons or holes, only from the trace of transient currents in the e-TOF measurement [18-22], which is carried out by applying step voltage instead of applying laser irradiation in the laser-TOF measurement. The best way to overcome this problem is to develop a technique that can directly probe traveling carriers themselves. Direct probing of the carrier motion itself is indeed helpful to discuss the detailed carrier transport mechanism in devices as well as in solid materials. However, this is impossible because electrons and holes are too small.

The Gauss law in the Maxwell's electromagnetic field theory [1,2,23] suggests an insightful idea for probing the carrier motion in materials. By probing the electric field associated with moving electrons and holes, the carrier motion can be visualized if the polarization induced in organic material surrounding the moving electrons and holes is probed. That is, we can probe carrier motion by probing dielectric polarization induced by the electric field arising from moving carriers. Time-resolved microscopic optical second harmonic generation (TRM-SHG) is a technique that enables us to probe the propagation of the dielectric polarization induced by electrons and holes which are moving across the organic materials, where nonlinear polarization induced in solids by coupling with incident electromagnetic waves e.g., laser beam, and *dc* electric field generated from moving carriers is probed in real time [24,25]. Furthermore, using a charge-coupled device (CCD) imaging system directly visualizes their motion. In this Topical review, we will discuss the technique to probe carrier motion in solids by using electric field induced optical second harmonic generation (EFISHG), and show our findings obtained by the EFISHG observation, e.g., carrier motions in organic field effect transistors (OFETs) [26,27], carrier behaviors in organic light emitting diodes (OLEDs) [28,29], Organic memory devices using ferroelectric layers [30,31], and Organic solar cells [32,33]. Noteworthy that, the idea of using EFISHG for the observation of carrier transport is based on the dielectric physics where *polarization* is a dominant parameter [34-36], and the EFISHG measurement for probing carrier

motions has been originally developed by the authors' group [36-40].

Finally we will stress that ideas and experiments based on the dielectric physics approach find a way for modeling and visualizing carrier motions in organic films and devices [37]. As we described above, probing carrier motions in solids is a fundamental research subject for electronics and material science. In this topical review, we show how dynamical carrier motions are allowed to be probed through detection of dielectric polarization phenomena originating from dipolar motions and electron transport, on the basis of MDC and EFISHG methods. These are electrical and optical methods, respectively, and basically different each other. However the concept of these two methods is the same in physics in that they are probing dynamical carrier motions through dielectric polarization phenomena. This is the most key reason why we here discuss the MDC and EFISHG measurements.

2. MDC, TOF and EFISHG methods

In this section, we make it clear the way for probing dynamical carrier motions by means of Time-resolved microscopic optical second harmonic generation (TRM-SHG), and also the way for probing dipolar motions by the MDC-measurement. We briefly discuss the time-of-flight (TOF) method for understanding the relationship between MDC and EFISHG measurements in section 2.2.

2.1 MDC measurement for probing dipolar motion

As mentioned in Sec. 1, in order to find a way to directly probe dynamical carrier motion in solids, it is very instructive to focus on the *dielectric polarization*. The dielectric polarization is given as sum of the spontaneous polarization, linear polarization, and nonlinear polarization [10,23,41]. Among them spontaneous polarization is generated when permanent dipoles align in the same direction, as illustrated in Fig. 1(a). For example, constituent rod-like polar molecules of Langmuir monolayers align on a water surface, pointing their long-axis direction towards air due to the symmetry breaking, and spontaneous polarization is thus generated in the monolayer [42-45]. According to the Gauss law, the electric flux density is arising from the constituent polar molecules with permanent dipoles. As a result, when we place a suspended electrode above the monolayers on a water surface, charges are induced on the electrode as shown in Fig. 1(b). The amount of induced charge is dependent on the orientational order of constituent rod-like polar molecules, and it can be described as [10-14,46]

$$Q_1 = -\frac{N\mu S_1}{L} - C\phi_s, \quad \text{with} \quad S_1 = <\cos\theta>. \tag{1}$$

Here N is the number of molecules under the suspended electrode, μ is dipole moment, and

L is the spacing between the suspended electrode and the water surface, and S_1 is the orientational order parameter which represents the average of tilt angle θ of constituent polar molecules [10]. ϕ_s is the surface potential of water subphase. C is the capacitance between the water surface and the suspended electrode. The MDC flows when charge Q_1 changes with time. Consequently, MDC is given in a manner as

$$I = \frac{d}{dt}Q_1 = \left[-\frac{B}{L}\left(\frac{d}{dt}P_z \right) - C\left(\frac{d}{dt}\phi_s \right) \right], \qquad (2)$$

where B is the electrode area of the suspended electrode, and P_z is the polarization of monolayer and given by $P_z = n\mu S_1$ with the surface density of molecules $n = N / B$. Presumably, the change of surface potential pressure ϕ_s is negligibly small by external stimuli, such as photoirradiation and monolayer compression. We therefore can pay more attention to the change of $P_z = n\mu S_1$ by external stimuli. P_z changes with n, μ and S_1. For example, n and S_1 change due to condensation and orientational ordering, respectively, in accordance with the occupied area per molecule, A ($n = 1/A$) by monolayer compression. μ changes due to phase transition of monolayer by compression. Further, for particular functional molecules, change of μ will be induced due to photo-isomerization etc. As mentioned above, P_z changes by external stimuli, but basically the change is related to the dynamical motion of dipoles such as rotational motion.

Figure 2 shows the MDCs generated from 4'-*n*-octyl-4-cyano-biphenyl (8CB) monolayers by monolayer compression, where the MDC is generated in accordance with the change of surface pressure by monolayer compression [14, 46-49]. Interestingly, the generation of MDC is very sensitive, because the MDC is transient current and it is generated only when the electric flux density between the suspended electrode and the monolayer changes with time. Actually, the

MDC is detectable even in the region of molecular area where the surface pressure is immeasurably very low (see region 1 in Fig. 2 where MDC is generated before initial rise of surface pressure during monolayer compression process). The details are as follows: the MDC current is described as

$$I = -\frac{B}{L}\left(\frac{d}{dA}P_z\right)\alpha = -\alpha\frac{B}{L}\left(-\frac{\mu S_1}{A^2} + \frac{\mu}{A}\frac{d}{dA}S_1 + \frac{S_1}{A}\frac{d}{dA}\mu\right) \text{ with } \alpha = \frac{d}{dt}A \ , \qquad (3)$$

assuming that change of ϕ_s is negligibly small during monolayer compression. In the MDC measurement, the experiments are carried out by monolayer compression with a constant compression speed α. From eq. (3), it is clear that MDC gradually changes in region 1 of Fig. 2(b), in accordance with the condensation of molecules and gradual change of orientational order $S_1 = <\cos\theta>$ by compression (1st and 2nd terms, respectively). On the other hand, the abrupt change of MDCs appears in regions 2 and 3 due to the change of polarization caused by phase transition (3rd term). Using eq. (3), we can determine the vertical component of permanent dipole moment of 8CB molecules, μS_1, as shown in Fig. 2(a).

Similarly, we can sensitively probe the change of molecular forms such as cis-trans photo-isomerization induced in azo-benzene monolayers by alternating photo-irradiation of ultra-violet and visible light [10,13, 50, 51]. The trans- and cis-form isomers have a permanent dipole μ_a and μ_b ($\neq \mu_a$), respectively. Accordingly, MDC is generated during the photo-isomerization process. The detection of photo-switching due to cis-trans photo-isomerization in monolayers on solids as MDC signals will be available as a basic principle of organic memory elements as shown in Fig. 3, where alternating ultra-violet (UV) and visible (Vis) light irradiation results in the generation of alternating MDC, whereas successive irradiation never generates MDC [13,51-53].

It is instructive here to note that surface potential method based on the Kelvin-probe method has been widely used for the study of monolayers at the air-water surface [54-56]. What we record by using this method is a compensation voltage V_c that is needed to make a zero-electric field between monolayer and the suspended electrode. That is, a compensation voltage V_c is applied to be $Q_1 = 0$ in the surface potential measurement. By adding the contribution of V_c to Eq. (1), we obtain the following equation:

$$Q_1 = -\frac{N\mu S_1}{L} - C\phi_s + CV_c = 0,$$

that is $V_c \approx +\frac{P_z}{\varepsilon_0} + \phi_s$. (4).

Here ε_0 is the dielectric constant of the air gap between the suspended electrode and monolayer, that is, nearly equals to the dielectric constant of vacuum. Eq. (4) tells us that the conventional surface potential measurement probes polarization P_z in accordance with the change of surface pressure by monolayer compression. In comparing eq. (4) with eq. (3), it is clear that the MDC measurement is very sensitive to the change of polarization P_z with molecular area A, while the surface potential measurement is not so sensitive. Actually it is very difficult to probe the change of polarization in the region before the initial rise of surface pressure by means of surface potential measurement. On the other hand, we can clearly see the generation of MDC current in this region, as shown in Fig. 2. Therefore, MDC measurement has an advantage in probing dynamical dipolar motions in monolayers.

2.2. TOF measurement for probing electron and hole transport

As mentioned in Sec. 1, in order to probe electron and hole transits across solids, time-of-flight measurement (TOF) is widely used [3-5,9]. To make it clear the difference of the TRM-EFISHG measurement with the TOF, we briefly discuss the basic concept of TOF. Figure 4(a) illustrates the situation of the TOF measurement, where charge $+q$ is placed between two electrodes 1 and 2, separated by organic layer with a thickness of d and connected to each other through an ammeter [5, 9]. Here this charge $+q$ is displaced from electrode 1, and it is located at a distance x from electrode 1. Owing to the neutrality of charge of this electrode arrangement system, the electric flux density arising from the charge $+q$ converges on electrodes 1 and 2 as follows:

$$q_1 = -\frac{d-x}{d}q, \quad q_2 = -\frac{x}{d}q \qquad (5)$$

The amount of induced charge q_1 and q_2 depends on the position x of the charge $+q$. If the charge $+q$ moves at a constant velocity $u(=dx/dt)$ in the direction from electrode 1

to electrode 2, the amount of charge q_1 and q_2 changes at a constant rate with time. Consequently, constant current $I = qu / d$ flows through the closed circuit whilst the charge $+q$ is being transported from the electrode 1 to electrode 2, as illustrated in Fig. 4(b). The transit time t_r is given by $t_r = d / u$, thus the total charge flowing through the circuit is $I \times t_r = q$. The current I flowing through the circuit is generated due to the change of electric flux density between electrode 1 (or 2) and charge $+q$, and this is nothing but the MDC current. Noteworthy, we here assumed that the charge $+q$ moves at a constant speed, thus it is possible to determine the position of charge from the trace of the $I-t$ curve. However, if the charge $+q$ does not move at a constant speed, it is not easy to determine the position of the charge $+q$, by using the $I-t$ curve.

In the conventional laser-TOF measurement, we give a *dc* voltage U on electrode 2 with respect to the grounded electrode 1 to form a constant electric field $E = U / d$ between the two electrodes during the measurement [5,17]. At $t = 0$, laser irradiation is employed to generate electron-hole pairs, only inside of the organic layer near the electrode 1. Consequently, only electrons can move from electrode 1 to electrode 2 at a velocity of $u = \mu_e E$ for $U > 0$, whereas only holes can move from electrode 1 to electrode 2 at a constant velocity of $u = \mu_h E$ for $U < 0$. Here, μ_e and μ_h are electron mobility and hole mobility, respectively. Presumably we define the transit time by the relations $t_r = d / u = d^2 / \mu_e U$ ($U > 0$) or $t_r = d^2 / \mu_h U$ ($U < 0$), and we measure the carrier mobility of holes and electrons by changing the polarity of the applied voltage U. This is the basic principle of the TOF measurement, and many experiments have been carried out for the determination of carrier mobility of polymers, insulators, organic semiconductors [5,18], etc., since the pioneering work of the carrier mobility measurement on anthracene crystals by Kepler [20]. In actual experiment, however, there are many problems. For example it is very difficult to irradiate laser beam only around the electrode 1, in particular, in the case of very thin films. Also space charge field caused by generated carriers distort the electric field distribution in the system and the carrier transport will be thus governed by this electric field. Furthermore, there is an upper limit on the transit time that can be measured in the TOF measurement, namely the ohmic relaxation time of

the film under test. That is, we cannot observe carrier transits in the region $t_r > t_{di}$ by using TOF, if carriers decay with the ohmic relaxation time t_{di}.

In the e-TOF measurement, the basic principle is the same as that used for the detection of MDCs. Instead of laser irradiation to generate electrons and holes, we apply a step voltage U to the two-electrode system to inject carriers from electrodes which transport between the two electrodes 1 and 2. As we probe the change of induced charges on electrodes along with the transport of injected carriers, this idea is easily extended to a three-electrode case such as field-effect transistors [20-22, 19], asymmetric needle-plane electrode system [57] and others, though the amount of induced charge on electrodes changes in a very complex manner, depending on the location of charges. Figure 5 shows an example of e-TOF measurement that is carried out for the determination of hole mobility in pentacene by using pentacene field effect transistors [20]. As we can see in the figure, the transient current abruptly flows at around the time when holes arrive at the counter electrode by crossing the channel. As shown in Fig.5, e-TOF measurement is helpful for the determination of carrier mobility of the materials, but it has a fundamental problem for the usage. We cannot determine the polarity of carriers merely from the trace of I-t curves, because positive and negative charges move along the electric field in the opposite directions each other. That is, the current is recorded as MDCs using an ammeter, but the MDC current is proportional to $+q\times(+u) = -q\times(-u)$ and we cannot distinguish the polarity of charge carriers. Therefore, we need to determine the carrier polarity using other methods, before we carry out the e-TOF measurement. As mentioned above, TOF measurement is helpful for the determination of carrier mobility, but this is under many physical boundary conditions.

2.3 TRM-EFISHG for visualization of electron and hole transport

The basic concept of TRM-EFISHG is different from the TOF measurement, and this technique basically allows us to distinguish electron and hole transports. To understand the EFISHG, we again go back to the Faraday's idea [2,23] formulated as the Gauss law. According to this law, electric field is arising from charges. We therefore postulate solids surrounding electrons and holes can be polarized. Actually, in the presence of non-zero *dc* electric field $E(0)$ by electrons and holes injected into organic solids, nonlinear polarization *P* is freshly induced when laser light is irradiated on solids, owing to the interaction between electromagnetic fields of the laser light and electrons in the organic materials. Figure 6 illustrates the basic principle of the EFISHG measurement [35,36]. Non-zero *dc* electric field $E(0)$ serves to distort electron cloud of molecules. As a result, this kind of nonlinear polarization *P* is induced even in centrosymmetric molecular systems, such as pentacene, phthalocyanine, C60 and others [41, 58-61]. Induced nonlinear polarization *P* is given as

$$P(2\omega) = \chi^{(3)}(2\omega;0,\omega,\omega)E(0)E_i(\omega)E_j(\omega) \quad , \qquad (6)$$

where $\chi^{(3)}(2\omega;0,\omega,\omega)$ represents the nonlinear optical susceptibility, ω stands for the angular wave frequency of incident electromagnetic wave, $E_i(\omega)$ and $E_j(\omega)$ represent the electric fields of laser, and $E(0)$ is the static electric field arising from moving-carriers, which satisfies the relation [1,2,23]

$$\nabla \cdot \vec{E}(0) = \frac{\rho}{\varepsilon_s \varepsilon_0} \quad , \qquad (7)$$

where ρ is the charge density of moving carriers, and ε_s and ε_0 are relative permittivity of the organic materials and the absolute permittivity of free space, respectively. The induced polarization $P(2\omega)$ is a source of second harmonic signal, and results in the enhancement of SH signal $I(2\omega)$ in proportion to the square of $P(2\omega)$, in a manner as

$$I(2\omega) \propto \left|P(2\omega)\right|^2 = \left|\chi^{(3)}(2\omega;0,\omega,\omega)E(0)E_i(\omega)E_j(\omega)\right|^2 . \qquad (8)$$

Here $I(2\omega)$ describes the SH intensity. From Eqs. (7) and (8), it is clear that the distribution of SH intensity in solids changes in accordance with the electric field distribution, i.e., non-linear polarization distribution. Consequently, by using a time-resolved EFISHG technique, we can directly observe carrier transport in solids by monitoring the propagation of polarization $P(2\omega)$ induced in the solids along with carrier motion [24,36]. Noteworthy that in the EFISHG measurement laser irradiation is used to generate nonlinear polarization, and it can be postulated that no photo carriers are generated. This is because the basic second harmonic generation process is a two-photon process, and the EFISHG process is similar to this two-photon process [59]. Consequently, we can measure carrier transport in solids and others in a non-destructive way. This is the characteristics of the EFISHG measurement, which differs from the laser-TOF measurement.

By the way, in electronic devices as well as in solids sandwiched between electrodes, there are many sources of *dc* electric fields. Among them are applying external voltage, moving carriers, trapped charges, work function difference and so forth. Consequently, the $E(0)$ in Eq.(8) is given by sum of the electric fields from many sources as [4,5]

$$E(0) = E_{ext}(0) + E_m(0) + E_t(0) + \cdots \quad . \tag{9}$$

Eq. (7) with Eq. (8) suggests that we can probe electric fields $E_{ext}(0), E_m(0), E_t(0)$ and others by using the EFISHG [29,62-68]. Time-resolved EFISHG method is particularly helpful for probing carrier motion in solids, as described in section 3. It is noteworthy that $\chi^{(3)}(2\omega;0,\omega,\omega)$ is a material dependent parameter, and it specifies the feature of materials. As a result, the SHG is activated at a specific wave length $\lambda_{2\omega} = 2\pi c/\omega$ (c, speed of light) of the materials, and this fact allows us to selectively probe SHG generated from one of the layer of multi-layers by choosing laser wavelength appropriately [62,69-71]. The magnitude of $\chi^{(3)}(2\omega;0,\omega,\omega)$ is very important in the EFISHG measurement. For example, the values of pentacene and C60 are in the order of 10^{-22} m^2/V^2 (10^{-14} esu) at laser wavelength of λ=1120 nm and 10^{-18} m^2/V^2 (10^{-10} esu) at λ=1000 nm [72], respectively, and EFISHG signals generated by laser light irradiation from Q-switched YAG laser with energy of 1mJ/pulse are probed as will be shown in Section 5. Note that these $\chi^{(3)}$ values are large due to the resonant coupling between the laser beam and electrons in molecules [73].

It should be noted that there are many reports on SHGs since the pioneering works by Bloembergen [74] and Shen [59]. Those works are focusing on molecular structure and chemicals from viewpoints of spectroscopy for characterizing material's structure. As a result, analysis of the SHG signal from non-symmetric chemical structures is the main topics. The SHG measurement employed in these works is different from the EFISHG measurement which we use here. Spectroscopic SHG experiments are carried out on focusing the SHG signal generated from materials in a form below,

$$I(2\omega) \propto \left|P^N(2\omega)\right|^2 = \left|\chi^{(2)}(2\omega;\omega,\omega)E_i(\omega)E_j(\omega)\right|^2 \quad , \tag{10}$$

where a main key parameter is material dependent $\chi^{(2)}(2\omega;\omega,\omega)$ parameter that depends on the arrangement of molecules and nonlinear susceptibility of molecules, but this is independent of the presence of *dc* field, $E(0)$. This situation is very helpful to characterize material structures, e.g., $\chi^{(2)}(2\omega;\omega,\omega)$ = 0 for symmetric molecular systems, such as pentacene and

C60. By choosing different light source with wavelengths ω_1 and ω_2 appropriately, sum frequency generation method is being carried out to precisely characterize material structures, dynamical change of orientational order of polar molecules, the interaction between molecules and surrounding solutions, and others (see text book [25,59] and review papers [75-77]). However, this situation is quite different from the Electric-field induced optical second harmonic generation (EFISHG) described by using Eq.(8), where *dc* field $E(0)$ makes a significant contribution by coupling with $\chi^{(3)}(2\omega;0,\omega,\omega)$. In other words, EFISHG is not activated if $E(0)=0.$ Probing $E(0)$ in Eq. (8) by means of EFISHG is indeed helpful for analyzing carrier behaviors and related electronic phenomena in organic devices. That is, we need to focus on the EFISHG process given by Eq. (8) to probe carrier motions and related electronic phenomena in electronic organic devices. As all of electric phenomena have some relation with carrier behaviors and thus EFISHG provides a way for analyzing carrier behaviors in devices, e.g., organic field effect transistors, organic solar cells, organic light emitting diodes, organic memory devices, etc., and also for analyzing electric field distribution in organic materials, etc. In the following sections, we discuss the Experimental systems and Examples of EFISHG measurements.

3. Experimental system of EFISHG measurement

Figure 7(a) shows the basic arrangement of the experimental system used for the measurement of carrier transport, where laser beam is vertically incident onto the sample through the objective lens, and emerged SHG images from the samples are captured with time by using a CCD camera [24,36]. The light source is an optical parametric oscillator, pumped by a third-harmonic light of Q-switched Nd:YAG laser (Continuum: SureliteII-10). To observe the carrier transport, we need to construct electrode arrangement appropriately. The most typical one is a planar type-OFET structure, where Source and Drain electrodes are placed to be parallel on the organic semiconductor layer, and the Gate electrode is placed on the substrate, as illustrated in the figure. Upon application of a step voltage, carriers are injected from Source or Drain electrode into the organic semiconductor layer, and they are then transported along the channel, i.e., between the two electrodes. Noteworthy that injection is dependent on the semiconductor materials and the electrode materials, but we can distinguish carrier species, i.e., electrons or holes, by SHG images [78-80]. Temporal resolution of the measurement system is limited by pulse width of laser and the rise time of voltage pulse. Thus, use of short pulse laser such as femto-second or pico-second laser is effective to reduce the pulse width of laser. On the other hand, there is further advantage of using short pulse lasers from the view point of the

nonlinear optical measurement. During the SHG measurement, we have to take care about the laser power to avoid damage of the sample. Sample damage is directly influenced by the pulse energy of laser, not instant optical power, whereas, SHG intensity is proportional to the instant optical power. Thus, use of short pulse laser is effective to observe the SHG signal without sample damage.

EFISHG is activated from the organic semiconductor layer by choosing a fundamental laser wavelength appropriately. For example, it was chosen at 1120 nm for studying pentacene-organic field effect transistors (OFETs) [81-84]. SH light generated from the semiconductor layer was filtered by a fundamental-cut filter and an interference filter to remove fundamental and other unnecessary light. Figure 7(b) illustrates an example of timing chart of the laser pulse and a step voltage applied to the OFET, which is used for the time-resolved EFISHG measurement. The parameter τ stands for the delay time, and by choosing the delay time τ we can visualize carrier motions at time $t = \tau$ after applying the step voltage at t=0. That is, using the visualized images, the change of electric field distribution along the OFET channel, corresponding to the carrier transport, is probed with time. That means from the visualized carrier motion we can distinguish injected carriers, i.e., electrons or holes.

At t = 0, upon application of a step voltage, carrier injection starts but still with no carrier injection into the semiconductor layer, while at $t = \tau$ injected carriers distribute along the channel of OFETs [85-88]. That is, we can directly visualize electric field distribution formed in the OFET by only external voltages by choosing τ =0, whereas we can map injected carrier distribution with time by choosing $\tau \neq 0$.

Noteworthy that EFISHG experiment is employed in the same way for sandwiched-type devices with two electrodes, by using laser beam that obliquely incident onto the devices [28,89-92]. Further we have recently developed a novel method that can detect electric field along the direction of incident laser beam by introducing a radial polarized beam into the EFISHG measurement system, and this system also makes us easy to study carrier transport in sandwiched-type devices [93,94].

One may concern about the generation of photo-carriers by irradiation of laser pulses that possibly affects the electrical properties of material. As mentioned, it can be neglected because the wavelength of fundamental light is far from the absorption peak. However, to satisfy the resonant condition a photon energy of SH light should be close to the optical gap. Then, we still need to take into account the photo-carrier generation by the two-photon absorption. Here we discuss the effect of two-photon absorption in C_{60} as an example. Two-photon absorption coefficient β of C_{60} was reported as 40 cm/GW at a wavelength of 1064 nm [95]. Assuming a typical Q-switched YAG laser with energy of 1mJ/pulse and a spot size of 1mm, a peak power

of the pulse is roughly estimated as 0.02 GW/cm^2. These parameters are substituted into $\Delta I = I_0(1 - e^{-\beta I_0 d})$ to evaluate the loss of optical power due to the two-photon absorption after passing through the C_{60} film with a thickness d of 100 nm. Then, we obtain $\Delta I = 8 \times 10^{-6}$. Accordingly, we neglect the effect of photo-carrier generation in the EFISHG measurement.

4. EFISHG images and Modeling

4.1 Carrier distribution and carrier motion

As described in section 2.2, we can measure electric field distribution in organic devices, carrier motion in organic devices, and others by probing non-linear polarization that results in EFISHG images. Firstly we discuss some examples and then discuss how carrier behaviors are modelled on the basis of experimental results.

a. Stationary-state

Since the discovery of conducting organic materials, organic devices have attracted much attention in electronics. Among them are organic light emitting diodes, organic field effect transistors, organic memory devices and so forth. In these electronic devices, organic semiconductors are used as active layers to realize their own device function, on the basis of general semiconductor device physics [96]. However, the carrier injection and transport mechanisms in actual organic devices are not so simple, owing to the dielectric nature of active organic layers. Basically, intrinsic carrier density is quite low in active organic layers. As a result, carrier injection process makes a dominant contribution. We can see such examples in organic field effect transistors and organic light emitting diodes, whose device performance are governed by the carrier injection process. This situation is very similar to the carrier transport in dielectric materials. Accordingly, it is a very effective way to directly measure electric field distribution changes in active layers in these organic devices for analyzing and modeling carrier behaviors. This is a dielectric physics approach that is helpful for analyzing carrier injection and transport of dielectric materials [4,5,9]. As already described in section 2, EFISHG measurement is capable of detecting electric field formed in organic devices due to static electric field by external applied *dc* voltage and time-varying electrostatic field by injected carriers. Keeping in mind this idea, electric field distribution formed along the channel of pentacene-OFETs has been measured. The electric field distribution formed in the pentacene-OFETs before and after hole injection into the channel has been well probed [81,97], and the electric field distribution before hole injection is shown in good agreement with the distribution analyzed using the rigorous solution of the Laplace field of the electrode system of OFETs [98,99]. Further the electric field distribution originated from injected carriers has been determined from the EFISHG measurements, and it has been shown that the charge distribution

along the OFET channel is basically determined based on a Maxwell-Wagner model that accounts for carrier accumulation at the interface between the gate-insulator/active organic layer interface [100,101].

Figure 8 shows a typical example of the EFISHG measurement that carried out for top-contact pentacene OFETs with Au Source and Drain electrodes [98]. Under the condition of no carrier injection of the OFETs, EFISHG is shown to be activated to satisfy the rigorous solution of the Laplace equation of a three-electrode system of the OFETs [98,99], as shown in Fig.8(a). On the other hand, under the condition of hole-injection, the intensity of EFISHG decreases due to the space charge field formed along the channel by injected holes, as shown in Fig.8(b) [97,99]. Using Eqs. (8) and (9), the carrier distribution along the channel is determined using the EFISHG measurement, as plotted in Fig.8(b). These results show that carrier accumulation along the channel is governed by the Maxwell-Wagner effect, and the distribution is basically determined based on a Maxwell-Wagner model [84,102,103]. Our further EFISHG study shows that the carrier distribution along the channel in steady-state that follows a solution of classical differential equation of current that describes continuity of carrier transport along the channel, which is modeled based on a transmission line model, as an extension of Maxwell-Wagner model [100,104]. Analytical results shows that the potential distribution along the channel is not linear, but it changes on satisfying the square root dependence along the channel, in a manner as [100,104]

$$V(x) = V_0\sqrt{1-\frac{x}{L}} \quad \text{with} \quad V(0) = V_0 \ \text{and} V(L) = 0, \tag{11}$$

where $x = 0$ and $x = L$ represents the edge of the source and the drain electrodes, respectively. Accordingly, the electric field distribution is given as

$$E(x) = \frac{V_0}{2\sqrt{L(L-x)}} \ . \tag{12}$$

EFISHG well probes this electric field distribution, and generates the signals that follow Eq.(8) with Eq. (12), where $E(0)$ of Eq.(8) is replaced by the $E(x)$ of Eq.(12).

As has been described above, it is clear that EFISHG is available for probing steady-state carrier distribution along the channel of OFETs. By the way, some organic materials show ambipolar behavior, which means that electrons and holes are allowed to enter into materials

from electrodes. In the field of electrical insulation engineering, this carrier behavior is called as double-injection [4]. Consequently probing electron and hole injection, and their distribution in organic devices is also important. For example, for organic light emitting device application, double carrier injection, i.e., electron and hole injection, is a key for device operation. Using ambipolar organic light emitting transistors (OLETs) with an active layer of the green-light-emitting polymer of poly9,9-di-n-octylfluorene-*alt*-benzothiadiazole (F8BT), which has a photo luminescent peak at the wavelength of 560 nm, the EFISHG measurement has been employed using a laser beam with a wavelength of 840 nm [79,101]. Of course, for the EFISHG experiment, we need to remove the influence of photoluminescence, by using a band pass filter so that we can probe the EFISHG that is generated at a wavelength of 420 nm only. The EFISHG experiments showed that there is actually a zero-potential position in the channel, which corresponds to the meeting point of electrons and holes for the electroluminescence [101].

b. transient carrier behavior

As mentioned in section 2, it is possible to probe carrier motion by means of the TRM-SHG. Using the electrode system illustrated in Fig.7, i.e., top-contact pentacene FETs with Au source and drain electrodes, TRM-SHG measurement has been carried out using OFETs with a channel length of 40 μm. Here the pentacene was deposited at room temperature, i.e., around 20 °C. Figure 9(a) shows the TRM-SHG image in the channel region of pentacene FET with 500 nm-thick SiO_2 gate insulator, where the SHG image was obtained along with carrier motions after a step positive voltage was applied. That is, positive voltage V_{pulse}=70 V was applied to the source electrode with respect to the gate and drain electrodes that were electrically shorted and grounded, i.e., $V_{ds} = V_{gs} = -70$ V. At τ = 0 ns, the laser pulse coincides with the rising edge of the voltage pulse, and SHG signals are found near the edge of Source electrode, indicating the Laplace electric field E_0, parallel to the channel, is formed only around the Source electrode. Interestingly, as is clearly shown in the image, the emission band of the SHG signal gradually moves in the channel from the Source to Drain electrode. The visualized emission band motion which starts from the source electrode evidently indicates hole-injection from the Au-Source electrode. That is, pentacene FET shows a *p*-type semiconductor behavior, where majority carriers are holes injected from the source electrode and the carrier mobility is 0.1–0.2 $cm^2\ V^{-1}\ s^{-1}$. Note that the SHG image appears only in the region within a radius of around 150 μm, owing to the spot-size of laser (see the region indicated by a circle in Fig. 9(a)). To further clarify the hole-transport mechanism across the channel, we plotted the SHG peak position with respect to the elapsed time, as shown in Fig. 9(b) [37,82,105]. From Figs. 9(a) and 9(b), it is clear that holes travel in the direction from the Source Au electrode to the Drain electrode, on

satisfying the square root time dependence [105,106]. This time dependence reflects the interface charge propagation process (see Fig. 9(b) and Ref. [100,107]), and well supports a Maxwell-Wagner effect model that is employed for analyzing transient carrier behaviors along the OFET channel. This is also well supported by a transmission line model that is basically based on the extension of the Maxwell-Wagner model. In physics, carriers propagate along the interface between gate insulator and active layer, and this situation is roughly described as that interface accumulated charge $Q_s = C_g(V_{gs} - V_{th} - \frac{V_{ds}}{2})$ spreads with a velocity of $v = \mu\bar{V}/L$, and thus illustrated by using a RC ladder circuit [100]. Here C_g is gate capacitor and V_{th} is threshold voltage. V_{gs} is the applied gate-source voltage and V_{ds} is the applied drain-source voltage and $\bar{V}$ ($\approx V_{gs} - V_{th} - V_{ds}/2$) is the average voltage for carrier drift in the FET channel region. In more detail, the transit time $t_{tr}(= L/v)$ is approximately given by [100]

$$t_{tr} \approx \frac{L^2}{\mu(V_{gs} - V_{th} - \frac{V_{ds}}{2})} \quad . \qquad (13)$$

Here μ is carrier mobility, and L is channel length. Eq. (13) suggests that the carrier migrates into the channel region on satisfying the square root time dependence. Computer simulation based on a classical drift-diffusion equation supports this prediction [106,108,109].

On the other hand, under the application of negative step voltage, the position of the SHG peak does not move, and the SHG signals are only concentrated around the edge of source electrode during the measurement. Results suggest that electron injection is minor and this process is negligible [26,110].

By the way, carrier injection is governed by the electrode materials and semiconductors. Accordingly the film preparation condition is very important, and we can prepare pentacene layers that exhibit ambipolar behavior by controlling the substrate temperature during the deposition of pentacene layers. Figure 10 (a) shows the I_{ds}-V_{gs} characteristics of pentacene FET with 500 nm-thick SiO_2 gate insulator, where the pentacene film was deposited at a substrate temperature of 70 °C and the channel length is 50 μm. An ambipolar behavior is seen in the I_{ds}-V_{gs} characteristics. That is, both electrons and holes are serving as carriers, depending on the applied V_{gs}. By employing the TRM-SHG experiment, we get the relationship between the position of carrier front with elapsed time by applying step voltage V_{gs}. Results show that the hole mobility is much higher than the electron mobility, i.e., about 100 times

higher, as portrayed in Fig.10(b) and 10(c) [111]. With consideration of these results, we can visualize the double carrier injection process that leads to recombination between electrons and holes injected from source and drain electrodes. Figure 11 shows the TRM-EFISHG experiment, where a negative step voltage of V_{dg}= -100 V was applied on the Drain electrode with respect to the gate, and on the Source electrode was applied a positive step voltage of V_{sg} = +100 V at the same time. As visualized in the images of Fig. 11, double carrier injection followed by the electron-hole recombination is clearly demonstrated. At the time corresponding to the carrier recombination, a bright band is seen due to the formation of high electric field between electrons and holes injected into the channel from the Drain and Source electrodes, respectively.

As shown in Fig.11, the TRM-EFISHG measurements allow us to visualize double carrier transport process, i.e., double carrier injection and recombination. Consequently, this technique is available for studying electro-light emitting process that starts from double carrier injection leading to carrier recombination, and also for visualizing the process that leads to pre-electrical breakdown in devices.

Further we should note that carrier propagation is dependent on the interfacial film condition of the channel, e.g., carrier traps, morphology, etc. Eq.(8) with Eq.(9) suggests that TRM-SHG is available for monitoring the contribution of the surface states of the channel. To confirm the potentiality of the TRM-SHG measurements, similar experiments were carried out for pentacene-FETs with 100 nm thick poly-methylmethacrylate (PMMA) layer on the surface of gate SiO_2 insulator [112,113]. The SHG intensity is concentrated in the front region of the propagating SHG profile [112]. Results indicate that space-charge field distribution is being formed along the channel due to trapping of holes. Analysis based on a carrier trap model well accounts for the TRM-SHG experiments. That is, TRM-SHG is effective to probe interface states of the channel region.

It is also noteworthy that the activation of EFISHG is material dependent, due to the material dependent parameter $\chi^{(3)}(2\omega;0,\omega,\omega)$ with angular frequency ω in Eq. (8). Consequently, probing carrier motion in one of layers in multi-layer systems is possible. Actually, we have already demonstrated the detection of such carrier motions in OFETs with an active layer of double-layer system, e.g., OFETs with a C60/pentacene active layer, etc [71,114,115], where the hole carrier transport in pentacene layer and electron carrier transport in C60 were selectively probed by choosing appropriate wavelengths of incident laser, which activate pentacene at 1120 nm and C60 at 1000 nm, respectively. That is, we can directly probe carrier motions in one of multilayers by choosing appropriate incident laser wavelength. The EFISHG measurement for pentacene/C60 OFETs showed that in C60 layer electrons are actually transport, etc.

c. Anisotropic carrier behavior

Carrier transport is strongly dependent on the film preparation condition, crystallinity of deposited films, and so forth. There are many film preparation methods, such as dipping-method, spin-coating method, evaporation method, and others. Accordingly anisotropic property is induced in deposited films, and the organic film shows the anisotropic carrier transport property; carrier transport along the long-molecular axis direction is different from the transport perpendicular to the long-molecular axis direction. To evaluate anisotropic carrier behavior is very important for the device technology, and also for understanding of carrier transport mechanism. By using the TRM-EFISHG measurement, we can visualize the anisotropic carrier transport behavior in organic thin films by using a round shape electrode system [116]. Figure 12 (a) shows the visualized SHG images by holes into Poly[(9,9-dioctylfluorenyl-2,7-diyl)-co-bithiophene]) (F8T2)-films from the edge of the round shape Au electrode. Here the F8T2 films were prepared using the floating film transfer method (FTM). As we can see in the set of figures (see Fig.12 (a-1), (a-2) and (a-3)), the spreading speed of holes from the edge of the round shape electrode is totally directional dependent on the film. As we can see in the distorted SHG image of injected holes around the Au edge of electrode, the carrier spreading is seen along the FTM direction, i.e., parallel to molecular long-axis direction of F8T2. On the other hand, the visualized carrier behavior of holes in pentacene films deposited by thermal evaporation is isotropic, as shown in Fig.12 (b-1), (b-2), (b-3). In this way, we can evaluate the anisotropic carrier behaviors by using the TRM-EFISHG microscopic images [116,117].

4.2 Carrier motion in sandwich-type devices

As mentioned in section 2, EFISHG measurement is available for measuring electric fields in the film-thickness direction as well as for probing carrier motions in sandwiched-type devices, most conventionally by introducing incident laser light obliquely onto such devices [28,90,118-121]. We here discuss topics related to the detection of electric field and carrier motions in film thickness direction.

Sandwich-type devices such as organic light-emitting diodes (OLEDs) and organic solar cells (OSCs) are designed on the basis of general semiconductor device physics. However, owing to the dielectric nature of organic semiconductor layers, the complexity of interfaces, the presence of traps, etc., it is quite a task to describe the energy diagram of actual organic devices. For example, organic double-layer diodes comprised of p- and n- type organic semiconductors show a rectification property, but actual potential distribution formed in these diodes is far different from the general semiconductor p-n diodes, owing to the dielectric nature of the organic

semiconductor layers [89]. Consequently, it is very effective to directly measure electric field and potential distributions in these devices for analyzing carrier behaviors in actual organic diodes [28,122]. We encounter similar situation when we talk about the rectification properties of MIS diodes using organic semiconductor layers [123,124]. As already discussed, EFISHG can directly and selectively probe electric field distribution in one of organic layers, and this technique also enables us to study carrier behaviors in organic sandwich-type devices [125-127]. Results of EFISHG are very helpful for determining the rectifying property of organic double-layer diodes, e.g., diodes with a structure of ITO/PI/TIPS-pentacene/Au [128,129].

a. Double layer EL diodes

Organic light-emitting diodes (OLEDs) have attracted much attention in electronics. Basically, an OLED is an injection-type device with two different electrodes that are separated by an organic multilayer [130]. Using energy diagram of molecules, e.g., HOMO and LUMO states, many researches have been carried out for improving the device performance [131]. Ideas of using low work function electrodes, depositing dipolar layers on the surface of electrodes, utilizing multilayer systems comprising hole- and electron-transport, electroluminescent layers, and so forth have been presented [131,132]. These important ideas are well accepted to achieve high-performance OLED devices [133]. However, owing to the ambiguities of energetics at the organic metal and organic-organic interfaces, carrier behavior in OLED devices is still not fully understood. To clarify the details, we need to pay attention to carrier injection from electrodes, carrier transport across active layers, and charge accumulation and recombination at the interface which lead to electroluminescence (EL). Hence, one of the most effective ways is to probe directly carrier motion in OLED devices. Probing carrier behaviors in combination with charge accumulation at the interface is particularly important, because the Maxwell-Wagner effect suggests carrier accumulation at the interface of layers, and this accumulation contributes to form space charge field. Consequently, EFISHG measurement coupled with the Maxwell-Wagner model analysis is very helpful for this purpose [28,29,89,134,135]. Making use of the TRM-EFISHG experiments on double layer OLEDs with *N,N'-di*-[(1-naphthyl)-*N,N'*-diphenyl]-(1,10-biphenyl)-4,4'-diamine (α-NPD) and tris (8-hydroxy-quinolinato) aluminum(III) (Alq3) layers by applying a step voltage showed well charging and discharging of carriers on electrodes and carrier transit across α-NPD and Alq3 layers, and non-reversal charging and discharging processes resulted from the different carrier behaviors accompanied by ordinary green EL [29,89].

To analyze carrier behaviors of this OLED devices, EFISHG measurement is carried out by laser irradiation with a wavelength of 820 nm, in order to selectively measure the electric field formed in the α-NPD layer by probing the SHG $I(2\omega)$ with a wavelength of 410 nm [28].

Upon application of external voltage $V_{ex}(t)$, the electric field across the α-NPD layer E_1 varies with time, on satisfying the following relation.

$$E_1(t) = \frac{C_2}{C_1 + C_2} \cdot V_{ex}(t) \cdot \frac{1}{d_1} - \frac{Q_s(t)}{C_1 + C_2} \cdot \frac{1}{d_1} + E_{1b} \qquad (14)$$

Here C_1 and C_2 are capacitance of α-NPD layer and Alq3 layer, respectively, d_1 is the thickness of α-NPD layer. E_{1b} is the electric field caused by work function difference etc, which corresponds to other terms in Eq. (8). $Q_s(t)$ is the interface charge accumulated at the interface between α-NPD and Alq3 layers owing to the Maxwell-Wagner effect. The EFISHG is given by Eq. (8) with $E_1(t)$ of Eq. (14), instead of $E(0)$. That is, the generated EFISHG changes on satisfying Eq. (14), showing that interface charge $Q_s(t)$ is accumulated with a response time governed by the Maxwell-Wagner relaxation time.

Figures 13 and 14 show, respectively, EL and EFISHG measurements under application of an *ac* square voltage to the ITO/α-NPD /Alq3/Al OLEDs [136,137]. Two kinds of *ac* square voltage waveforms are chosen, one is with no *dc* components (Square voltage *a*), and the other is with *dc* components (Square voltage *b*). As Figure 13 shows that EL is generated in accordance with the applied *ac* square voltage, where the generation is dependent on the applied frequency and also the wave form. In more detail, the EL intensity gradually decays with the increase of the frequency of the applied *ac* square voltage, and reaches a minimum at the frequency corresponding to the carrier transit time of Alq3 layer. Interestingly, the EL intensity again increased by the application of further higher frequency *ac* square voltages, relying on the *dc* component of the *ac* square voltages [138-140]. Results suggest the presence of two EL modes, where the space charge field caused by the interface charge makes a significant contribution. That is, in the low frequency region, accumulated holes at the interface suppress hole injection and leads to the decrease of the EL intensity activated by the recombination of holes and electrons injected from opposite electrodes. On the one hand, in the high frequency region, the accumulated holes assist electron injection and result in the increase of EL intensity activated by the recombination of the interfacial accumulated holes and injected electrons from

Al electrode. However these are merely speculation, and we need to make clear the presence of this space charge field caused from accumulated interface charges and its contribution. For this purpose EFISHG measurement is useful. Figure 14 shows the EFISHG measurements in the low frequency region, where two kinds of *ac* square voltage waveforms are chosen, i.e., one with no *dc* component (Square voltage *a*), the other with *dc* component (Square voltage *b*) [136-138]. From the top to bottom, the applied external voltage, $V_{ex}(t)$, generated EFISHG intensity $I(2\omega)$, electric field $E_1(t)$ and accumulated interface charge $Q_s(t)$ are plotted. Here generated EFISHG intensity $I(2\omega)$ is plotted by $\sqrt{I(2\omega)}$ with consideration of the relation between the electric field and generated EFISHG (see Eq. (8)). $Q_s(t)$ is calculated using the Gauss law of Eq. (7) with the EFISHG equation (8). Under *ac* voltage application with no *dc* component (Square voltage *a*), in region A, Q_s is zero, in prior to voltage application V_{ex}=+20 V. In region B, external voltage V_{ex}=+20 V induces charges on the ITO and Al electrodes with a circuit response time $t_{RC}(=RC)\sim10^{-7}$ s, and form electric field in the α-NPD layer as high as $E_{RC}=5.6\times10^5$ V/cm. After that, in region C, holes are injected from ITO to α-NPD layer and electrons are injected from Al to Alq3 layer for radiative EL recombination. The holes smoothly transport in α-NPD layer (hole mobility: $\mu_h\sim10^{-4}$ cm^2/Vs) but electrons go through Alq3 layer slowly (electron mobility: $\mu_e\sim10^{-5}$ cm^2/Vs), due to imbalance of hole and electron transport in the layers. As the result, holes excessively accumulate at the α-NPD/Alq3 interface, and the electric field in the α-NPD layer decreases. The EFISHG showed that the electric field actually decreases from $E_{RC}=5.6\times10^5$ V/cm to $E_{Qs}=4.8\times10^5$ V/cm at $t_d=10^{-5}$ s due to excess hole accumulation $Q_s=6.5\times10^{-8}$ C/cm^2.On the other hand, under *ac* voltage application with *dc* component (Square voltage *b*), electrode charges are induced on the ITO and Al electrodes and holes excessively accumulated at the α-NPD/Alq3 interface, in the way similar to the carrier processes under the Square voltage *a*. However, excess holes stayed at the α-NPD/Alq3 interface in regions A and E $Q_s^0=3.0\times10^{-8}$ C/cm^2, as evidenced by the EFISHG measurement. These results support the prediction that there are accumulated holes at the interface, and these charges suppress hole injection in the low frequency region and lead to the decrease of the EL intensity. Using the EFISHG results, we can carry similar discussion on the presence of interface charge and its contribution, in terms of the EL in the high frequency region [137,140]. In this way, we can monitor dynamical carrier behaviors in charging and discharging processes in EL devices, by means of EFISHG.

Noteworthy that, electroluminescence has been received much attention as one of the

pre-breakdown phenomena in the field of electrical insulation engineering for past several ten years, where the main research interest is to detect very weak EL signals for the diagnostics of insulators. However, using EFISHG provides a new way for the detection of the pre-breakdown phenomena because carrier motions leading to carrier recombination can be monitored, as shown in Fig.15 [141].

b. Double layer memory devices.

Ferroelectric polymers are widely used as memory materials, where copolymer of vinylidene fluoride (VDF) and trifluoroethylene (TrFE), P(VDF-TrFE) stands out as its bistable and remanent polarization that can be repeatedly turn-over by an external electric field [142,143]. Recently, ferroelectric polymers have also been used in electronic devices such as organic field effect transistors (OFETs) [144,145] and organic photovoltaic cells (OPVs) [146,147], where a strong internal electric field induced in the active layer of these devices by spontaneous polarization of ferroelectric polymers is well utilized for efficient device operations. As a result, carrier behaviors in the active semiconductor layer, e.g., pentacene, have been deeply studied in terms of the turn-over of spontaneous polarization of ferroelectric layer [148,149]. For the p-type pentacene OFETs with a ferroelectric P(VDF-TrFE) gate insulator, hole/electron injection, transportation, charging, and discharging at the P(VDF-TrFE) gate insulator interface and so forth have been clarified in response to the turn-over of spontaneous polarization of ferroelectric layer. Similarly organic memory MIS diodes with a ferroelectric P(VDF-TrFE) insulator have been studied. These studies are mainly carried out by means of electrical measurements such as displacement current measurement (DCM) using ramp voltage [150,151], but these are no longer sufficient to account for carrier behaviors in a variety of organic semiconductor devices being utilized with ferroelectric P(VDF-TrFE) layers. Using EFISHG probes the electric field change induced in organic devices with a ferro-electric layer gives much information on the carrier behavior in these devices [152-154].

Figure 16 shows a typical example of DCM measurements for MFM and MFSM (the inset of Fig. 16(a)) devices, which were prepared on patterned indium zinc oxide (IZO) substrates [30]. P(VDF-TrFE) (72-28 mol. %) layer with a thickness of 200 nm was spin-coated on the substrate, and then pentacene layer (200 nm, for MFSM device) and gold electrode were thermally evaporated successively. For the DCM measurement, a ramp voltage was applied on the IZO electrode. Figure 16(a) shows the results of DCM for the MFM device. Two peaks (peaks A and B) are clearly observed at symmetric positions at voltages corresponding to the coercive electric field E_c of 0.6 MV/cm, and show no dependence on sweeping frequencies of ramp voltage. These results suggest that the appearance of peaks A and B are due to the turn-over of spontaneous polarization.

On the other hand, for MFSM devices, three peaks A, B, and C are clearly observed. The appearance of the third peak, peak C, at the non-symmetric position of peak A is a typical characteristic of the MFSM device. Results suggest a two-step polarization reversal of ferro-electric layer in the pentacene/P(VDF-TrFE) double-layer device. However this is merely a speculation. For studying carrier behaviors with the turn-over of polarization, it is very helpful to measure the electric field formed in pentacene and PVDF layers. Figure 17 shows the result of EFISHG measurement, where the electric field across pentacene layer is recorded [31]. Results clearly verify the proposed two step polarization reversal process by the two different hysteresis loops: one loop is in Fig.17 corresponding to peak A and B, and the other loop is corresponding to peak C [148]. Results of EFISHG suggest that the interaction of interfacial charge and ferroelectric polarization is responsible for this two-step process. Noteworthy that situation of the 2-step turn- over strongly depends on organic semiconductor materials, where the interaction at the interface between ferroelectric layer and semiconductor layer is quite different. For example, for P(VDF-TrFE) /C60/Au(or Al) double layer devices, only two peaks appear, but the peak position appears at quite different voltages from those of P(VDF-TrFE) /pentacene /Au double layer device, owing to the potential drop across C60 layers. Using the EFISHG measurement is an effective way for clarifying the contribution of organic semiconductor layers [153,155].

c. Organic solar cells

There are many kinds of organic solar cells (OSCs), e.g., bilayer type, blended-type, etc. Among them bulk hetero-junctions (BHJs) OSCs have been paid much attention, in terms of the conversion efficiency of OSCs. Using BHJs, an idea of the introduction of hole and electron blocking layers has also been developed. However the basic mechanism of carrier behavior is getting more and more complex. Thus development of techniques available for probing carrier behaviors in OSCs is anticipated, for getting the whole picture of carrier behaviors.

In BHJs OSCs, electron donor and acceptor molecules are mixed to introduce larger contacting area for creating excitons to be separated into electrons and holes efficiently. However it is very speculative to identify carrier paths in such devices. The EFISHG measurement is very useful to investigate fundamental processes, not only in bilayer (double active layer) OSCs but also in blended-type OSCs [156-160]. Main reason is that the generation of the EFISHG depends on the materials properties of targeted sample. Consequently, it is possible to observe and study different material components in the BHJ layer individually, by choosing two appropriate laser wavelengths. This is an advantage of the EFISHG for the study of carrier path in BHJ OSCs. For example, for OSCs co-deposited with pentacene and C60, EFISHG measurement has been carried out at two laser wavelengths of 1000 nm and 860 nm,

by which carrier behavior inside the pentacene and C60 have been selectively probed. As a result, the presence of two carrier paths for electrons and holes have been identified from the EFISHG response by application of laser pulse to the OSCs [63]. The EFISHG provides an additional promising method to study carrier path of electrons and holes as well as dissociation of excitons in BHJ OSCs [161,162]. Further recently much attention has been focused on the perovskite solar cells, where the dissociation of excitons is postulated to happen in the bulk of the solar cells. We believe that the EFISHG can be employed to make clear the contribution of the internal electric field, and thus the technique is available for studying the carrier process.

As mentioned above, EFISHG is available for studying carrier behaviors in organic devices. Finally we should note that this method has a potentiality to study carrier behaviors in inorganic devices, such as amorphous silicon (a-Si) solar cells [163] and AlGaN/GaN high electron mobility transistors (HEMT) [164,165].

5. Conclusions

In this review paper, we summarized novel methods for studying carrier motions in solids and in devices by probing polarization induced in organic materials. The methods are MDC and EFISHG measurements. In both measurements, *polarization* is a key parameter for the detection of dynamical carrier motions. In the MDC measurement, we probe *polarization* induced by orientationally aligned dipoles, by measuring the change of induced charge on electrodes with time. On the other hand, in the EFISHG measurement, *nonlinear polarization* induced in solids in the presence of dc electric field is probed by coupling with a laser beam. As carriers are source of electric fields, we anticipate that EFISHG is broadly available for studying electronic devices. As mentioned above, by focusing on *polarization* induced by dipoles, and electrons and holes, we find a way to analyze dynamical carrier motion in solids and in devices. As a future scope, we also need to study a way for probing dynamical motions caused by quadrupoles, and others. Further we need to couple MDC and EFISHG measurements with other methods that can probe carrier motions in energy space. Coupling of charge modulation spectroscopy, electro-absorption spectroscopy, and others will be effective [115,166-169]. Further experiments and studies proceed.

Acknowledgement

A part of this work was financially supported by a Grant-in-Aid for Scientific Research (Nos. 01550239, 22226007, 24360118, 25709022, 22760227) from Japan Society for the Promotion of Science.

References

1) Maxwell J C 1954 *A Treatise on Electricity and Magnetism* (New York: Dover) 3rd edn.
2) Collin R E 1960 *Field Theory of Guided Waves* (New York: McGraw-Hill)
3) Meier H 1974 *Organic Semiconductors: Dark- and Photoconductivity of Organic Solids* (Weinheim: Verlag Chemie)
4) Lampert M A and Mark P 1970 *Current Injection in Solids* (New York: Academic)
5) Sessler G M 1980 *Electrets* (Berlin: Springer)
6) Hilczer B and Małecki J 1986 *Electrets* Studies in Electrical and Electronic Engineering, Vol. 14 (Amsterdam, Oxford, New York, Tokyo: Elsevier, Warszawa: PWN-Polish Scientific Publishers)
7) Chen R and Kirsh Y 1979 *Analysis of Thermally Stimulated Processes* (Oxford: Pergamon Press)
8) Turnhout J V 1975 *Thermally Stimulated Discharge of Polymer Electrets* (New York: Elsevier)
9) Iwamoto M and Taguchi D 2014 *Thermally Stimulated Current in Electrical and Electronic Materials, Analysis and Application* (Tokyo: Corona-sha). [in Japanese]
10) Iwamoto M and Wu C X 2000 *The Physical Properties of Organic Monolayers* (Singapore: World Scientific)
11) Iwamoto M and Majima Y 1988 *Jpn. J. Appl. Phys.* **27** 721
12) Majima Y and Iwamoto M 1990 *Jpn. J. Appl. Phys.* **29** 564
13) Iwamoto M, Majima Y, Naruse H, Noguchi T and Fuwa H 1991 Nature **353** 645
14) Iwamoto M and Majima Y 1991 *J. Chem. Phys.* **94** 5235
15) Iwamoto M, Wu C X and Kim W Y 1996 *Phys. Rev. B* **54** 8191
16) Miller G and Grasser T 2010 (ed) *Organic Electronics*, Advances in Polymer Science, Vol. 223 (New York: Springer)
17) Kepler R G 1960 *Phys. Rev.* **119** 1226
18) Köhler A and Bässler H 2015 *Electronic Processes in Organic Semiconductors: An Introduction* (Weinheim: Wiley), Chap. 3, pp. 193-306.
19) Basu D and Dodabalapur A 2010 Drift Velocity and Drift Mobility Measurement in Organic Semiconductors Using Pulse Voltage *Organic Electronics*, Advances in Polymer Science, Vol. 223 ed Meller G and Grasser T (Heidelberg, Dordrecht, London, New York: Springer)
20) Weis M, Lin J, Manaka T and Iwamoto M 2009 *J. Phys. Chem. C* **113** 18459
21) Dost R, Das A and Grell M 2008 *J. Appl. Phys.* **104** 084519
22) Lin J, Weis M, Taguchi D, Manaka T and Iwamoto M 2011 *Jpn. J. Appl. Phys.* **50** 04DK01

23) Feynman R P, Leighton R B and Sands M 1964 *The Feynman Lectures on Physics II* (MA, Addison-Wesley)
24) Manaka T, Lim E, Tamura R and Iwamoto M 2007 *Nat. Photonics* **1** 581
25) Motti S G, Maia F C B and Miranda P B 2014 Nonlinear Spectroscopy of Interfaces and Its Application to Organic Electronics *Ultrafast Dynamics in Molecules, Nanostructures and Interfaces*, Series in Optics and Photonics, Vol. 8, ed Gurzadyan G G, Lanzani G, Soci C and Sum T C (Singapore: World Scientific)
26) Manaka T, Lim E, Tamura R and Iwamoto M 2005 *Appl. Phys. Lett.* **87** 222107
27) Taguchi D, Masada H, Manaka T, Iwamoto M, Nishiura T, Iizuka T and Takemori T 2012 *Org. Electron*. **13** 2801
28) Taguchi D, Weis M, Manaka T and Iwamoto M 2009 *Appl. Phys. Lett*. **95** 263310
29) Taguchi D, Zhang L, Li J, Weis M and Manaka T and Iwamoto M 2010 *J. Phys. Chem. C* **114** 15136
30) Li J, Taguchi D, Ouyang W, Manaka T and Iwamoto M 2011 *Appl. Phys. Lett.* **99** 063302
31) Li J, Weis M, Taguchi D, Manaka T and Iwamoto M 2012 *J. Appl. Phys*. **111** 023706
32) Taguchi D, Shino T, Chen X, Zhang L, Li J, Weis M, Manaka T and Iwamoto M 2011 *Appl. Phys. Lett.* **98** 133507
33) Taguchi D, Shino T, Chen X, Zhang L, Li J, Weis M, Manaka T and Iwamoto M 2011 *J. Appl. Phys.* **110** 103717
34) Iwamoto M, Manaka T and Lim E 2009 in *Encyclopedia of Applied Spectroscopy*, ed Andrews D L (Weinheim: Wiley-VCH) Chap. 23, p. 817
35) Iwamoto M, Manaka T, Yamamoto T and Lim E 2008 *Thin Solid Films* **517** 1312
36) Iwamoto M, Manaka T, Weis M and Taguchi D 2010 *J. Vac. Sci. Technol. B* **28** C5F12
37) Iwamoto M, Manaka T and Taguchi D 2014 *Jpn. J. Appl. Phys.* **53** 1000101 (Invited Review paper)
38) Li C Q, Manaka T, Cheng X M and Iwamoto M 2002 *J. Appl. Phys.* **92** 6390
39) Lim E, Taguchi D and Iwamoto M 2014 *Curr. Appl. Phys.* **14** 1156
40) Iwamoto M, Manaka T and Taguchi D *Visualizing Carrier Motion in Organic Devices by Electric Field Induced Optical Second Harmonic Generation* 2015 Display and Imaging, in press.
41) Boyd R W 2008 *Nonlinear Optics* 3rd edn (Amsterdam: Academic)
42) Ulman A 1995 (ed) *Organic Thin Films and Surfaces: Directions for the Nineties* Thin Films Vol. 20 (San Diego, New York, Boston, London, Sydney, Tokyo, Toronto: Academic Press)
43) Roberts G G and Pitt C W 1983 (ed) *Langmuir-Blodgett Films, 1982* Thin Films Science and Technology, Vol. 3 (Amsterdam, Oxford, New York: Elsevier)

44) Fukuda K and Sugi M 1989 (ed) *Langmuir-Blodgett Films 4* Vol. 1-3 (London, New York: Elsevier)
45) Thin Solid Films, special issue Vol. 178 No.1-2. Proceedings of the 4th International Conference on Langmuir-Blodgett Films, Tsukuba, Japan April 24-29, 1989.
46) Sugimura A, Iwamoto M and OuYang Z C 1994 *Phys. Rev. E* **50** 614
47) Iwamoto M, Kubota T and OuYang Z C 1996 *J. Chem. Phys.* **104** 736
48) Iwamoto M, Kubota T and Muhamad M R 1995 *J. Chem. Phys.* **102** 9368
49) Wu C X and Iwamoto M 1998 *Phys. Rev. E* **57** 5740
50) Iwamoto M, Kanai Y and Naruse H 1993 *J. Appl. Phys.* **74** 1131
51) Iwamoto M, Majima Y, Naruse H and Iriyama K 1992 *J. Appl. Phys.* **72** 1631
52) Naruse H, Iwamoto M, Yokoyama S, Kakimoto M and Imai Y 1994 *Thin Solid Films* **242** 220
53) Naruse H, Ohnishi K, Iwamoto M, Ichimura K, Seki T, Tamaki T and Iriyama K 1993 *Jpn. J. Appl. Phys.* **32** 2832
54) Gaines G L 1966 *Insoluble Monolayers at Liquid-Gas Interfaces* (New York: Interscience)
55) Petty M C 1990 Characterization and Properties *Langmuir-Blodgett Films* ed Roberts G (New York: Plenum Press) Chap. 4, pp. 133-222.
56) Ulman A 1991 An Introduction to Ultrathin Organic Films from Langmuir-Blodgett to Self-Assembly (Boston, San Diego, New York, London, Sydney, Tokyo, Tronto: Academic Press) Chap. 1.1
57) Iwamoto M, Fukuzawa F and Hino T 1987 *IEEE Trans. Electr. Insul.* **EI-22** 419
58) Manaka T, Li C Q, Cheng X M and Iwamoto M 2004 *J. Chem. Phys.* **120** 7725
59) Shen Y R 1984 *The Principles of Nonlinear Optics* (New York: Wiley)
60) Li C Q, Manaka T, Cheng X M and Iwamoto M 2003 *Jpn. J. Appl. Phys.* **42** 2516
61) Manaka T, Suzue Y and Iwamoto M 2005 *Jpn. J. Appl. Phys.* **44** 2818
62) Chen X, Taguchi D, Manaka T and Iwamoto M 2012 *J. Appl. Phys*. **111** 113711
63) Chen X, Taguchi D, Manaka T and Iwamoto M 2014 *Appl. Phys. Lett.* **104** 013306
64) Zhang L, Taguchi D, Li J, Manaka T and Iwamoto M 2010 *J. Appl. Phys.* **108** 093707
65) Zhang L, Taguchi D, Manaka T and Iwamoto M 2011 *J. Appl. Phys*. **110** 033715
66) Lee K, Weis M, Lin J, Taguchi D, Majková E, Manaka T and Iwamoto M 2011 *J. Appl. Phys*. **109** 064512
67) Bazaka K, Jacob M V, Taguchi D, Manaka T and Iwamoto M 2011 *Chem. Phys. Lett*. **503** 105
68) Manaka T, Kohn H, Ohshima Y, Lim E and Iwamoto M 2007 *Appl. Phys. Lett.* **90** 171119
69) Zhang L, Taguchi D, Manaka T and Iwamoto M 2011 *Appl. Phys. Lett.* **99** 083301

70) Lim E, Taguchi D and Iwamoto M 2011 *Chem. Phys. Lett*. **515** 306
71) Shibata Y, Nakao M, Manaka T, Lim E and Iwamoto M 2009 *Jpn. J. Appl. Phys.* **48** 021504
72) Kajzar F, Taliani C, Danieli R, Rossini S and Zamboni R 1994 *Chem. Phys. Lett.* **217** 418
73) Verbiest T, Clays K and Rodriguez V 2009 *Second-Order Nonlinear Optical Characterization Techniques: An Introduction* (New York: CRC), Chap. 5 and 6
74) Bloembergen N 1965 *Nonlinear Optics* (New York: W. A. Benjamin)
75) Sung W, Kim D and Shen Y R 2013 Sum-frequency vibrational spectroscopic studies of Langmuir monolayers *Curr. Appl. Phys.* **13** 619 (Review paper)
76) Miranda P B and Shen Y R 1999 Liquid Interfaces: A Study by Sum-Frequency Vibrational Spectroscopy *J. Phys. Chem. B* **103** 3292 (Feature Article)
77) Tian C S and Shen Y R 2014 Recent progress on sum-frequency spectroscopy *Surf. Sci. Rep.* **69** 105
78) Mir I A, Ahuja T, Kumar D, Taguchi D, Manaka T and Iwamoto M 2010 *Synth. Met*. **160** 2116
79) Ohshima Y, Lim E, Manaka T, Iwamoto M and Sirringhaus H 2011 *J. Appl. Phys*. **110** 013715
80) Nakao M, Manaka T, Weis M, Lim E and Iwamoto M 2009 *J. Appl. Phys.* **106** 014511
81) Manaka T, Lim E, Tamura R, Yamada D and Iwamoto M 2006 *Appl. Phys. Lett*. **89** 072113
82) Lim E, Manaka T, Tamura R and Iwamoto M 2006 *Jpn. J. Appl. Phys.* **45** 3712
83) Weis M, Lin J, Taguchi D, Manaka T and Iwamoto M 2010 *Appl. Phys. Lett*. **97** 263304
84) Tamura R, Lim E, Manaka T and Iwamoto M 2006 *J. Appl. Phys.* **100** 114515
85) Manaka T, Liu F, Weis M and Iwamoto M 2009 *Appl. Phys. Express* **2** 061501
86) Zhang L, Taguchi D, Masada H, Manaka T and Iwamoto M 2012 *Jpn. J. Appl. Phys.* **51** 02BK08
87) Abe Y, Taguchi D, Manaka T and Iwamoto M 2013 *Thin Solid Films* **554** 166
88) Satou H, Ohshima Y, Kohn H, Manaka T and Iwamoto M 2011 *J. Appl. Phys.* **109** 054506
89) Taguchi D, Inoue S, Zhang L, Li J, Weis M, Manaka T and Iwamoto M 2010 *J. Phys. Chem. Lett.* **1** 803
90) Taguchi D, Shino T, Zhang L, Li J, Weis M, Manaka T and Iwamoto M 2011 *Appl. Phys. Express* **4** 021602
91) Chen X, Taguchi D, Lee K, Manaka T and Iwamoto M 2011 *Chem. Phys. Lett*. **511** 491
92) Chen X, Taguchi D, Lee K, Manaka T and Iwamoto M 2013 *Jpn. J. Appl. Phys.* **52** 04CR05
93) Taguchi D, Manaka T, Iwamoto M, Karasuda T and Kyomasu M 2013 *Jpn. J. Appl. Phys*. **52** 04CK04
94) Sadakata A, Yano R, Taguchi D, Manaka T and Iwamoto M 2014 *Trans. Mat. Res. Soc. Japan* **39** 443

95) Lindle J R, Pong R G S, Bartoli F J and Kafafi Z H 1993 *Phys. Rev. B* **48** 9447
96) Sze S M 1981 *Semiconductor Device Physics* (New York: Wiley) 2nd edn
97) Lim E, Manaka T and Iwamoto M 2007 *J. Appl. Phys*. **101** 024515
98) Yamada D, Manaka T, Lim E, Tamura R, Weis M and Iwamoto M 2008 *J. Appl. Phys*. **104** 74502
99) Yamada D, Manaka T, Lim E, Tamura R and Iwamoto M 2008 *J. Appl. Phys*. **103** 84118
100) Weis M, Lin J, Taguchi D, Manaka T and Iwamoto M 2010 *Jpn. J. Appl. Phys*. **49** 071603
101) Mashiko Y, Taguchi D, Weis M, Manaka T and Iwamoto M 2012 *Appl. Phys. Lett*. **101** 243302
102) Weis M, Taguchi D, Manaka T and Iwamoto M 2010 *Jpn. J. Appl. Phys.* **49** 04DK15
103) Weis M, Lin J, Taguchi D, Manaka T and Iwamoto M 2010 *Jpn. J. Appl. Phys.* **49** 071603
104) Weis M, Manaka T and Iwamoto M 2009 *J. Appl. Phys.* **105** 24505
105) Manaka T, Liu F, Weis M and Iwamoto M 2008 *Phys. Rev. B* **78** 121302
106) Manaka T, Liu F, Weis M and Iwamoto M 2009 *J. Phys. Chem. C* **113** 10279
107) Weis M, Lin J, Taguchi D, Manaka T and Iwamoto M 2009 *J. Phys. Chem. C* **113** 18459
108) Liu F, Lin J, Manaka T and Iwamoto M 2011 *J. Appl. Phys.* **109** 104512
109) Noma T, Taguchi D, Manaka T and Iwamoto M 2015 *IEICE Trans. Electron.* **E98-C** 86
110) Lim E, Manaka T and Iwamoto M 2007 *J. Appl. Phys*. **101** 024515
111) Manaka T, Nakao M, Lim E and Iwamoto M 2009 *Materials Science-Poland* **27** 709
112) Manaka T, Liu F, Weis M and Iwamoto M 2010 *J. Appl. Phys.* **107** 043712
113) Tanaka Y, Manaka T and Iwamoto M 2011 *Chem. Phys. Lett.* **507** 195
114) Taguchi D, Manaka T and Iwamoto M 2015 Kogaku **44** 111 [in Japanese]
115) Zhang L, Taguchi D, Manaka T and Iwamoto M 2012 *Appl. Phys. Lett*. **100** 103301
116) Manaka T, Matsubara K, Abe K and Iwamoto M 2013 *Appl. Phys. Express* **6** 101601
117) Matsubara K, Manaka T and Iwamoto M 2015 *Appl. Phys. Express* **8** 041601
118) Taguchi D, Sumiyoshi R, Chen X, Manaka T and Iwamoto M 2014 *Thin Solid Films* **554** 51
119) Taguchi D, Chen X, Manaka T and Iwamoto M 2013 *Mol. Cryst. Liq. Cryst.* **578** 50
120) Taguchi D, Manaka T, Iwamoto M, Anderson L J and Jacob M V 2014 *Chem. Phys. Lett.* **593** 69
121) Jacob M V, Bazaka K, Taguchi D, Manaka T and Iwamoto M 2012 *Chem. Phys. Lett.* **528** 26
122) Taguchi D, Zhang L, Li J, Weis M, Manaka T and Iwamoto M 2011 *Jpn. J. Appl. Phys*. **50** 04DK08
123) Lim E, Taguchi D and Iwamoto M 2013 *Chem. Phys. Lett*. **561-562** 97
124) Lim E, Taguchi D and Iwamoto M 2014 *Organic Electron.* **15** 3590

125) Taguchi D, Manaka T, Iwamoto M, Bazaka K and Jacob M V 2013 *Chem. Phys. Lett.* **150** 572

126) Zhang L, Taguchi D, Li J, Manaka T and Iwamoto M 2011 *Appl. Phys. Lett*. **98** 092109

127) Zhang L, Taguchi D, Li J, Manaka T and Iwamoto M 2011 *Jpn. J. Appl. Phys.* **50** 04DK13

128) Lim E, Taguchi D and Iwamoto M 2013 *Org. Electron*. **14** 1903

129) Lim E, Taguchi D and Iwamoto M 2012 *Org. Electron*. **13** 2489

130) Tang C W and VanSlyke S A 1987 *Appl. Phys. Lett*. **51** 913

131) Salaneck W R, Seki K, Kahn A, Pireaux J-J 2002 (ed) *Conjugated Polymer and Molecular Interfaces* (New York: Marcel Dekker)

132) Brütting W and Adachi C 2012 (ed) *Physics of Organic Semiconductors* (Weinheim: Wiley-VCH)

133) Tsujimura T 2012 *OLED Display Fundamentals and Applications*, Wiley Series in Display Technology (New Jersey: Wiley)

134) Weis M, Otsuka T, Taguchi D, Manaka T and Iwamoto M 2015 *Charge injection and accumulation in organic light-emitting diode with PEDOT:PSS anode, J. Appl. Phys.* accepted

135) Sadakata A, Yano R, Taguchi D, Manaka T and Iwamoto M 2014 *Trans. Mat. Res. Soc. Japan* **39** 443

136) Sadakata A, Taguchi D, Yamamoto T, Fukuzawa M, Manaka T and Iwamoto M 2011 *J. Appl. Phys.* **110** 103707

137) Sadakata A, Osada K, Taguchi D, Yamamoto T, Fukuzawa M, Manaka T and Iwamoto M 2012 *J. Appl. Phys.* **112** 083723

138) Sadakata A, Yamamoto T, Taguchi D, Manaka T, Fukuzawa M and Iwamoto M 2012 *Mol. Cryst. Liq. Cryst*. **567** 187

139) Sadakata A, Oda Y, Taguchi D, Fukuzawa M, Manaka T and Iwamoto M 2013 *Jpn. J. Appl. Phys*. **52** 05DC03

140) Sadakata A, Osada K, Taguchi D, Manaka T and Iwamoto M 2014 *Thin Solid Films* **554** 110

141) Taguchi D, Nakamoto R, Manaka T and Iwamoto M 2014 *Jpn. J. Appl. Phys*. **53** 04EK02

142) Koga K and Ohigashi H 1986 *J. Appl. Phys.* **59** 2142

143) Tajitsu Y, Ogura H, Chiba A and Furukawa T 1987 *Jpn. J. Appl. Phys*. **26** 554

144) Tamura R, Yoshita S, Lim E, Manaka T and Iwamoto M 2008 *Jpn. J. Appl. Phys*. **47** 3170

145) Yoshita S, Tamura R, Taguchi D, Weis M, Lim E, Manaka T and Iwamoto M 2009 *J. Appl. Phys*. **106** 024505

146) Yuan Y, Reece T J, Sharma P, Poddar S, Ducharme S, Gruverman A, Yang Y and

Huang J 2011 *Nature Mat*. **10** 296

147) Weis M, Li J, Taguchi D, Manaka T and Iwamoto M 2011 *Appl. Phys. Express* **4** 121601

148) Li J, Taguchi D, Manaka T and Iwamoto M 2012 *Jpn. J. Appl. Phys*. **51** 02BK07

149) Li J, Zhang L, Ou-Yang W, Taguchi D, Manaka T and Iwamoto M 2010 *Jpn. J. Appl. Phys*. **49** 121601

150) Asadi K, Blom P W M and de Leeuw D M 2011 *Appl. Phys. Lett.* **99** 053306

151) Kalbitz R, Gerhard R and Taylor D M 2012 *Org. Electron.* **13** 875

152) Cui X, Taguchi D, Manaka T and Iwamoto M 2014 *Jpn. J. Appl. Phys*. **53** 02BB05

153) Cui X, Taguchi D, Manaka T and Iwamoto M 2013 *J. Appl. Phys*. **114** 234504

154) Cui X, Taguchi D, Manaka T, Pan W and Iwamoto M 2013 *Org. Electron*. **15** 537

155) Lee K, Weis M, Chen X, Taguchi D, Manaka T and Iwamoto M 2014 *Thin Solid Films* **554** 189

156) Chen X, Taguchi D, Shino T, Manaka T and Iwamoto M 2011 *J. Appl. Phys.* **110** 074509

157) Chen X, Taguchi D, Manaka T and Iwamoto M 2014 *Org. Electron*. **15** 2014

158) Chen X, Taguchi D, Weis M, Manaka T and Iwamoto M 2012 *Jpn. J. Appl. Phys.* **51** 041605

159) Chen X, Taguchi D, Manaka T and Iwamoto M 2012 *Org. Electron*. **14** 320

160) Chen X, Taguchi D, Manaka T and Iwamoto M 2014 *Thin Solid Films* **554** 158

161) Ahmad Z, Abdullah S M, Taguchi D, Sulaiman K, Manaka T and Iwamoto M 2014 *Laser Phys.* **24** 105701

162) Ahmad Z, Abdullah S M, Taguchi D, Sulaiman K and Iwamoto M 2015 *J. Appl. Phys.* **117** 163101

163) Ou-Yang W, Manaka T, Naitou S, Kunitomo K, Iwamoto M 2012 *Jpn. J. Appl. Phys.* **51** 070209

164) Katsuno T, Manaka T, Ishikawa T, Ueda H, Uesugi T and Iwamoto M 2014 *Appl. Phys. Lett.* **104** 252112

165) Katsuno T, Manaka T, Ishikawa T, Ueda H, Uesugi T and Iwamoto M 2014 *Microelectron. Reliab.* **54** 2227.

166) Manaka T, Kawashima S, Iwamoto M 2010 *Appl. Phys. Lett.* **97** 113302

167) Zhang L, Taguchi D, Manaka T and Iwamoto M 2013 *Jpn. J. Appl. Phys*. **52** 05DC01

168) Lim E, Taguchi D and Iwamoto M 2014 *Appl. Phys. Lett.* **105** 073301

169) Miyazawa R, Taguchi D, Weis M, Manaka T and Iwamoto M 2010 *Jpn. J. Appl. Phys.* **49** 04DK07

Figure captions

Figure 1: (*a*) Permanent dipole of polar molecule and spontaneous polarization due to alignment of dipoles. (*b*) Maxwell Displacement current (MDC) measurement and aligned polar molecules at the water surface. The charge Q_1 is induced on the suspended top electrode, which is a source for MDC current.

Figure 2: (*a*) Dipole moment of polar molecules estimated from MDC measurement. (*b*) MDC current during monolayer compression. (*c*) Surface pressure-area isotherm during monolayer compression.

Figure 3: MDC due to photo-isomerization of azobenzene monolayer. The trans- and cis-conformation change of azobenzene induced the reversible MDC signals [13].

Figure 4: (*a*) The space charge $+q$ and induced charges q_1 and q_2 on the electrodes. (*b*) TOF current that flows during transit of charge $+q$. The current flows only in the time $0 < t < t_r$.

Figure 5: TOF measurement of pentacene field effect transistors with various transistor channel length (L=40, 50, 60, 80, 100 μm). In the measurement, holes are injected from the Source electrode at t = 0, transported across the transistor channel region, and arrived at the Drain electrode at the time indicated by arrows. Reprinted with permission from Weis M, Lin J, Taguchi D, Manaka T and Iwamoto M 2009 *J. Phys. Chem. C* **113** 18459 [20]. Copyright 2009 American Chemical Society.

Figure 6: The generation of electric-field-induced optical second-harmonic generation (EFISHG) light. In the presence of electrostatic field $E(0) \neq 0$, electron clouds in molecules are distorted and the nonlinear polarization $P(2\omega)$ is produced. As a result, EFISHG is emitted from molecules with its intensity $I_{2\omega} \propto |P_{2\omega}|^2$.

Figure 7: (*a*) The time-resolved microscopic SHG (TRM-SHG) measurement system that can visualize carrier propagation in organic field-effect transistors and others. As a light source, pulsed lasers such as Nd:YAG and femto laser are available. (*b*) Timing chart of *dc* voltage V_{gs} and V_{ds}, and pulsed laser incidence, for TRM-SHG measurements.

Figure 8: (*a*) The electrostatic field (Laplace field) formed in the pentacene field-effect transistor. The black curve is the electric field distribution which was directly visualized by TRM-SHG measurement. The thick gray curve is a numerical calculation by a finite element method. Reprinted with permission from Yamada D, Manaka T, Lim E, Tamura R, Weis M and Iwamoto M 2008 *J. Appl. Phys.* **104** 074502 [98]. Copyright 2008, AIP Publishing LLC. (*b*) The electric field distribution at the Drain electrode edge of pentacene field-effect transistor. The filled circles and open squares plot electric field distributions with and without hole injection, under *dc* voltage application to the Gate electrode with reference to the Au Source electrode (V_{gs} < 0). Yamada D, Manaka T, Lim E, Tamura R and Iwamoto M 2008 *J. Appl. Phys.* **103** 084118 [99]

Figure 9: (*a*-1) The TRM-SHG image of holes propagating in the pentacene field-effect transistor. The top and bottom region of the image is the Drain and Source electrodes, while the center region is the transistor channel (L=40 μm). Upon voltage application to V_{gs} (<0) at τ=0 s, holes are injected from the Source electrode edge to the channel. (*a*-2)-(*a*-7) The EFISHG images visualize the injected holes propagating to the Drain electrode. The carrier front of the holes, indicated by arrows, shift from the Source to the Drain as the time τ elapsed after *dc* voltage application. (*b*) The motion of carrier front position from the Source electrode edge. Holes propagates along the transistor channel on satisfying $x \propto \sqrt{\tau}$ relation, indicating that carrier drifting governs the carrier transport mechanism [37]. Copyright (2014) The Japan Society of Applied Physics.

Figure 10: (a) I_{ds}-V_{gs} curve of the ambipolar pentacene field-effect transistor. Reprinted from Manaka T, Kawashima S and Iwamoto M 2011 Charge modulation spectroscopy for probing ambipolar carrier injection into pentacene field effect transistors *Physics Procedia* **14** 209. Copyright (2011), with permission from Elsevier. (b) TRM-SHG images directly visualizing hole (left) and electron (right) transport in the ambipolar pentacene field-effect transistor. Holes and electrons are injected from the Source electrode edge by the voltage application V_{gs}<0 and V_{gs}>0, respectively. The carrier propagating front, indicated by arrows, shift from the Source to the Drain as the time τ elapsed. (c) Time dependence of the carrier front position from the Source electrode edge, for holes and electrons moving in the pentacene OFET channel.

Figure 11: TRM-SHG measurement of ambipolar pentacene OFET. (a) SHG image visualizing carrier motion of both holes and electrons. (b) Experimental setup for pulse voltage application to OFETs. Electrons were injected from the Drain electrode in prior to hole injection from the Source electrode. (c) SHG intensity profile across the OFET channel from Source electrode edge (0 μm) to the Drain electrode edge (40 μm). The SHG peak corresponding to the frontier

of propagating holes meet electrons at around 33 μm. The enhanced local electric field due to hole-electron recombination process is clearly observed in the bottom profile (400 ns).

Figure 12: (*a*-1)-(*a*-3) The anisotropic hole transport in F8T2 film prepared by the FTM method. The holes are injected from the round-shaped single electrode, and transported in the film with maximum carrier mobility μ_{max} and μ_{min} as illustrated. EFISHG images clearly suggested that hole mobility is high in the FTM direction [indicated by an arrow in (*a*-3)], reflecting anisotropic F8T2 film formed by the film preparation process. $\vec{E}_{\omega}$ in (*a*-1) indicates polarization direction of the incidence laser beam. (*b*-1)-(*b*-3) The isotropic hole transport in pentacene film prepared by the conventional vacuum evaporation. TRM-SHG visualized the isotropic carrier transport of the pentacene film, reflecting isotropic morphology of the pentacene film by vacuum evaporation.

Figure 13: EL intensity curve as a function of frequency of square wave voltage. The blue squares show EL under voltage with no *dc* component (Square voltage *a*), while red circles plot EL under voltage application with non-zero *dc* voltage component (Square voltage *b*).

Figure 14: EFISHG measurement of ITO/α-NPD/Alq3/Al double-layer OLED, under application of voltage with and without *dc* component. (*a*) Square-root of the SHG intensity $\sqrt{I_{2\omega}}$. (*b*) Electric field in the α-NPD layer estimated from the SHG intensity. (*c*) Interfacial charge Q_s accumulating upon voltage applications.

Figure 15: EFISHG-*t* measurement that detects instantaneous charging of OLED (device structure: IZO/α-NPD/Alq3/Al) as a pre-electrical breakdown phenomena. Result showed that (1) SH intensity is stable after *dc* voltage was applied to OLED at *t*=50 s, (2) SH intensity occasionally and instantaneously enhanced due to charging in prior to electrical breakdown at *t*=560 s, as indicated by an arrow, (3) electrical breakdown occured at *t* = 600 s. In the measurement, electric field in the α-NPD layer was probed for detecting pre-electrical breakdown phenomena, by using the probing laser beam with a wavelength of 820 nm.

Figure 16: Displacement current measurement of organic memory devices under triangular voltage application. (*a*) MFM structure device [IZO/P(VDF-TrFE)/Au]. (*b*) MFSM structure device [IZO/P(VDF-TrFE)/pentacene/Au]. Reprinted with permission from Li J, Taguchi D, OuYang W, Manaka T and Iwamoto M 2011 *Appl. Phys. Lett.* **99** 063302 [30]. Copyright 20011, AIP Publishing LLC.

Figure 17: EFISHG measurement of the MFSM type memory device. Result shows hysteresis behavior of memory device. Loop 1 is the first-step polarization reversal of peak B in the DCM, while loop 2 is the second-step polarization reversal of peak C. (*a*) Electric field change estimated based on the Maxwell-Wagner effect model. (*b*) Electric field directly probed by the EFISHG measurement. Reprinted with permission from Li J, Weis M, Taguchi D, Manaka T and Iwamoto M 2012 Analyzing a two-step polarization process in a pentacene/poly(vinylidene fluoride-trifluoroethylene) double-layer device using Maxwell-Wagner model *J. Appl. Phys.* **111** 023706 [31]. Copyright 2012, AIP Publishing LLC.

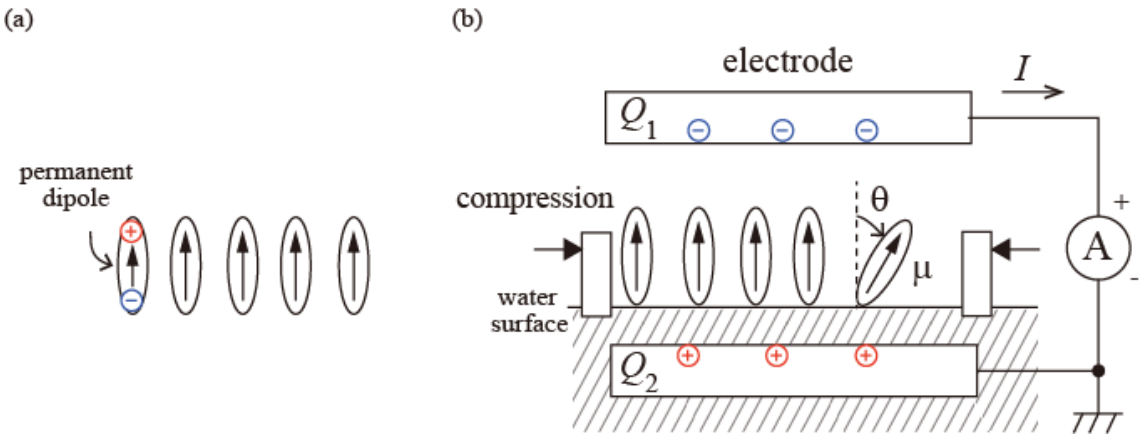

Figure 1: M. Iwamoto et al.

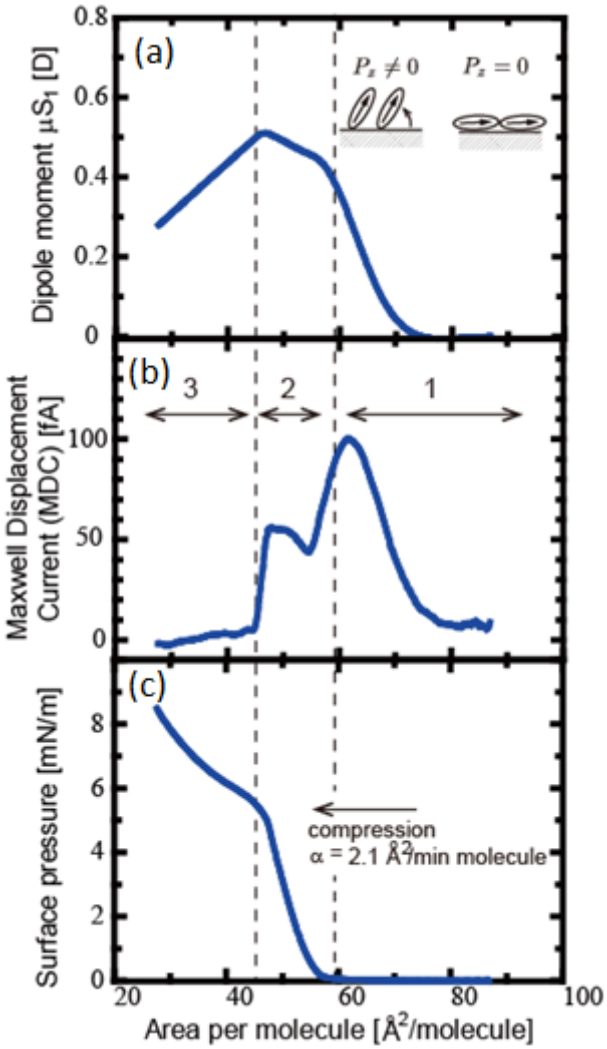

Figure 2: M. Iwamoto et al.

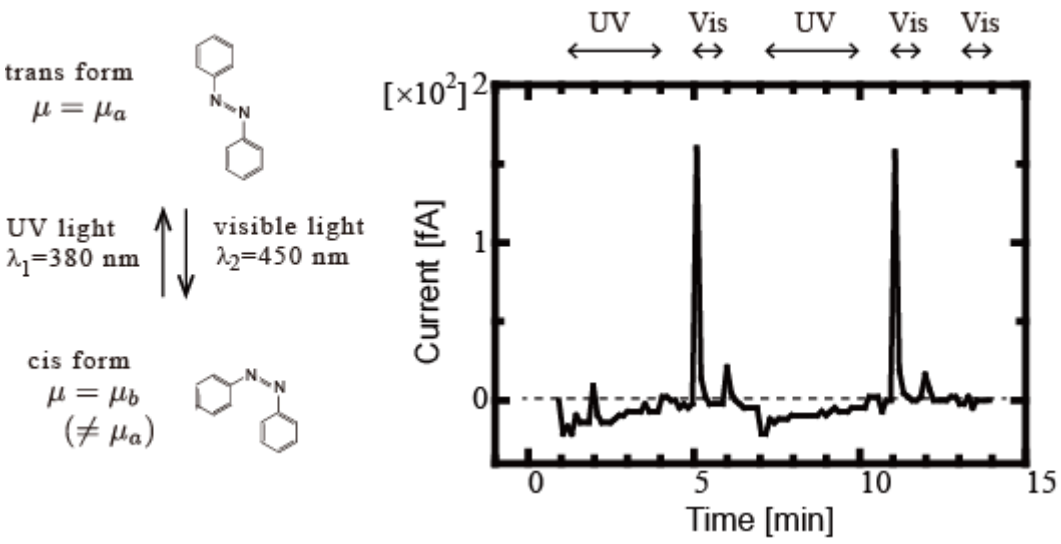

Figure 3: M. Iwamoto et al.

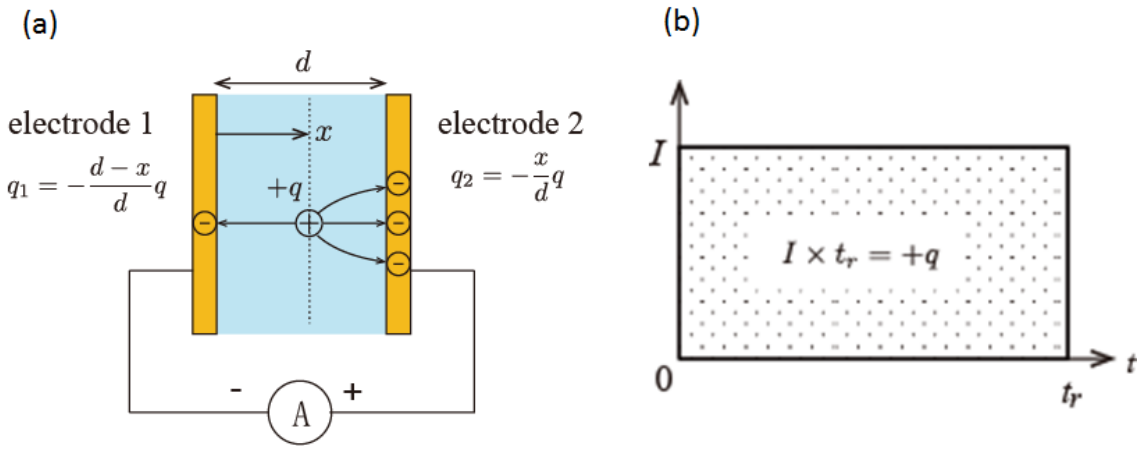

Figure 4: M. Iwamoto et al.

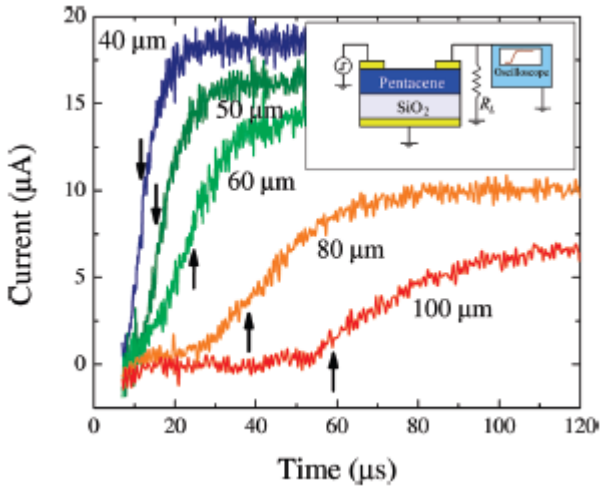

Figure 5: M. Iwamoto et al.

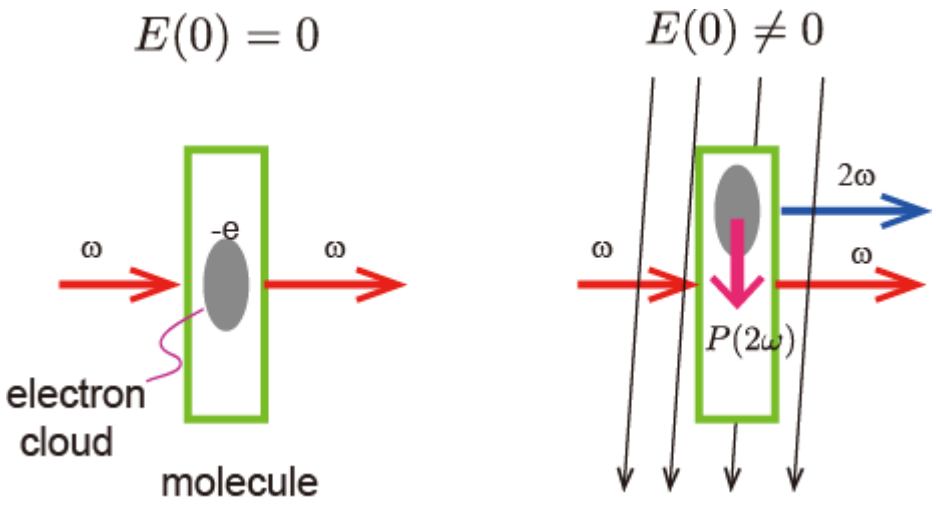

Figure 6: M. Iwamoto et al.

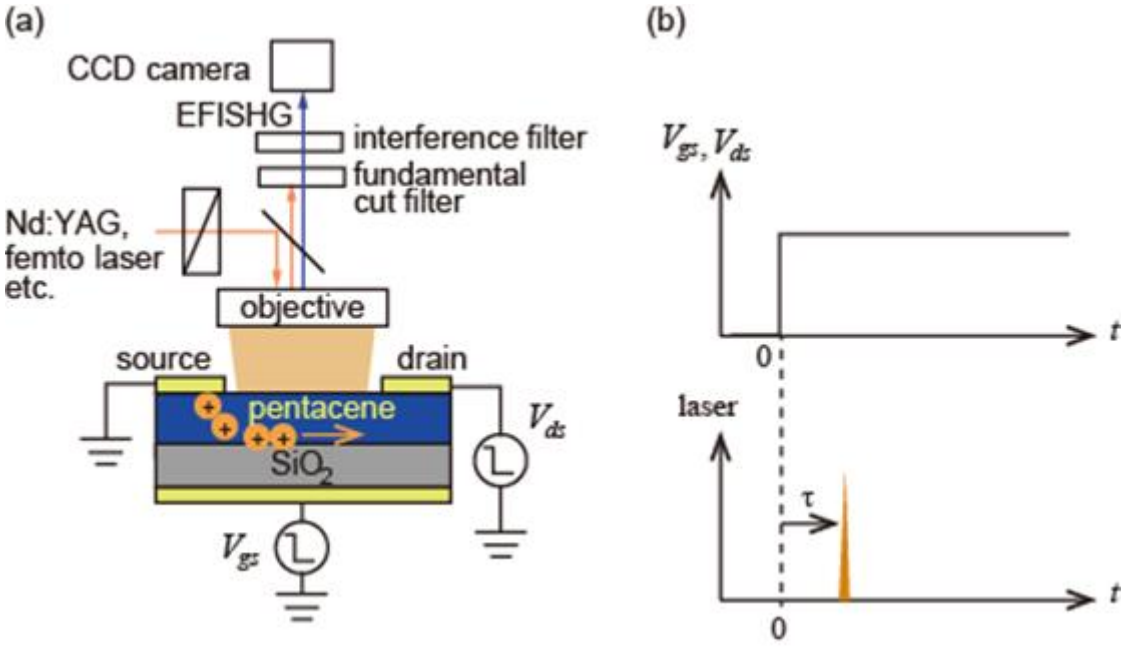

Figure 7: M. Iwamoto et al.

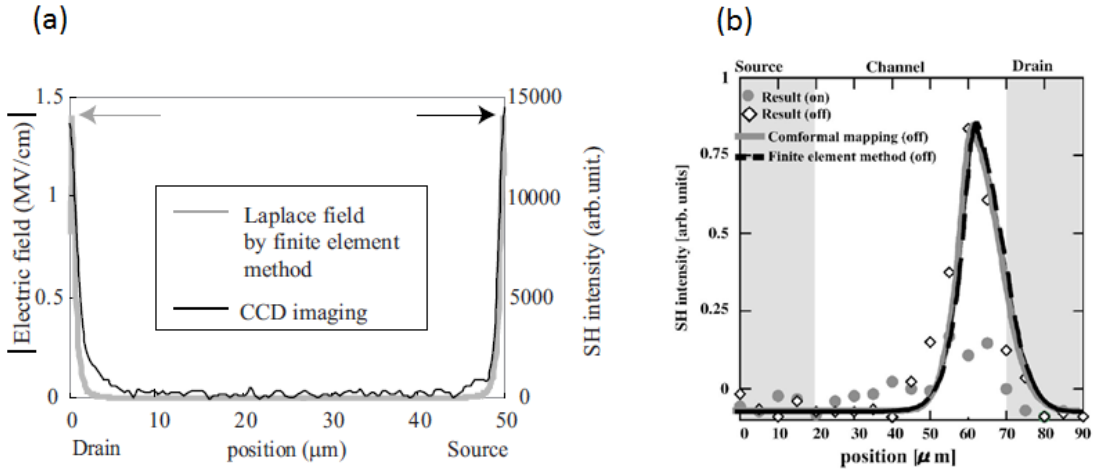

Figure 8: M. Iwamoto et al.

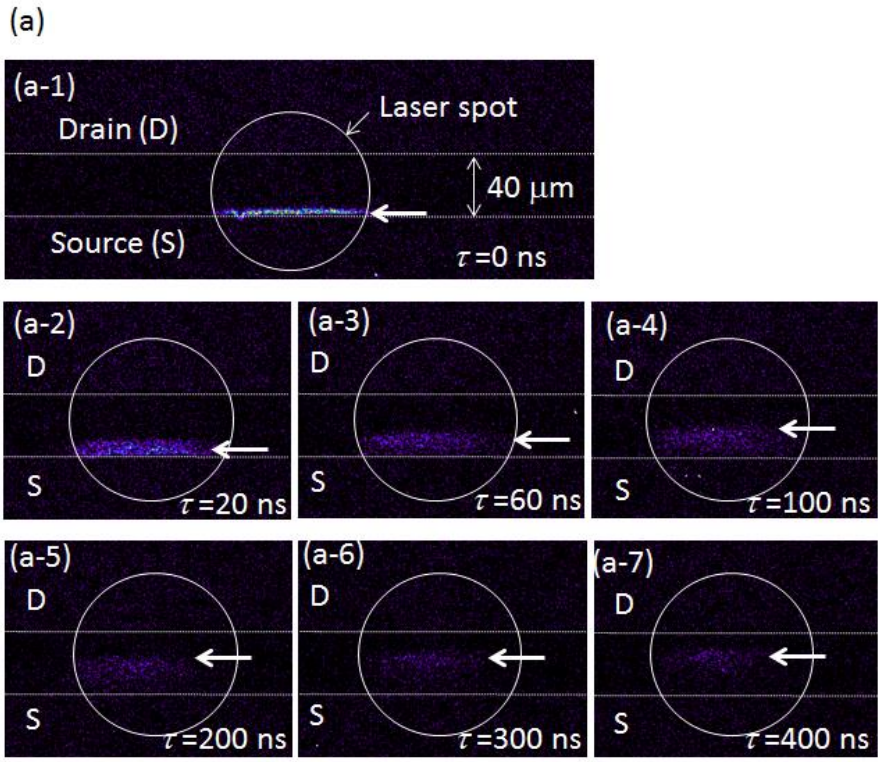

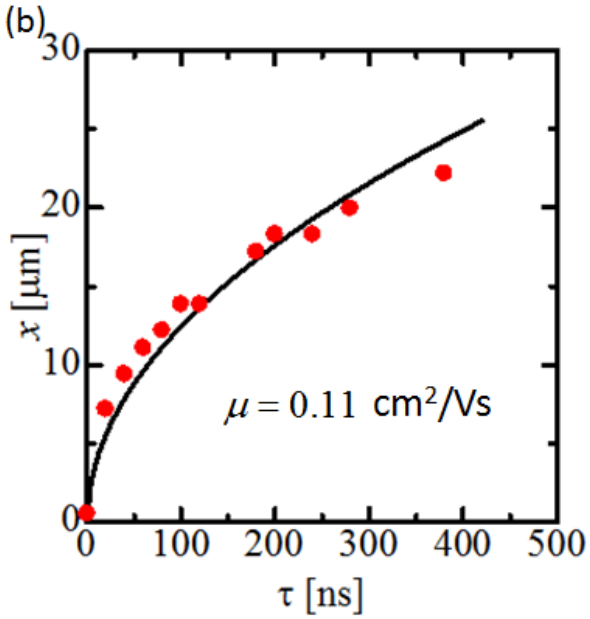

Figure 9: M. Iwamoto et al.

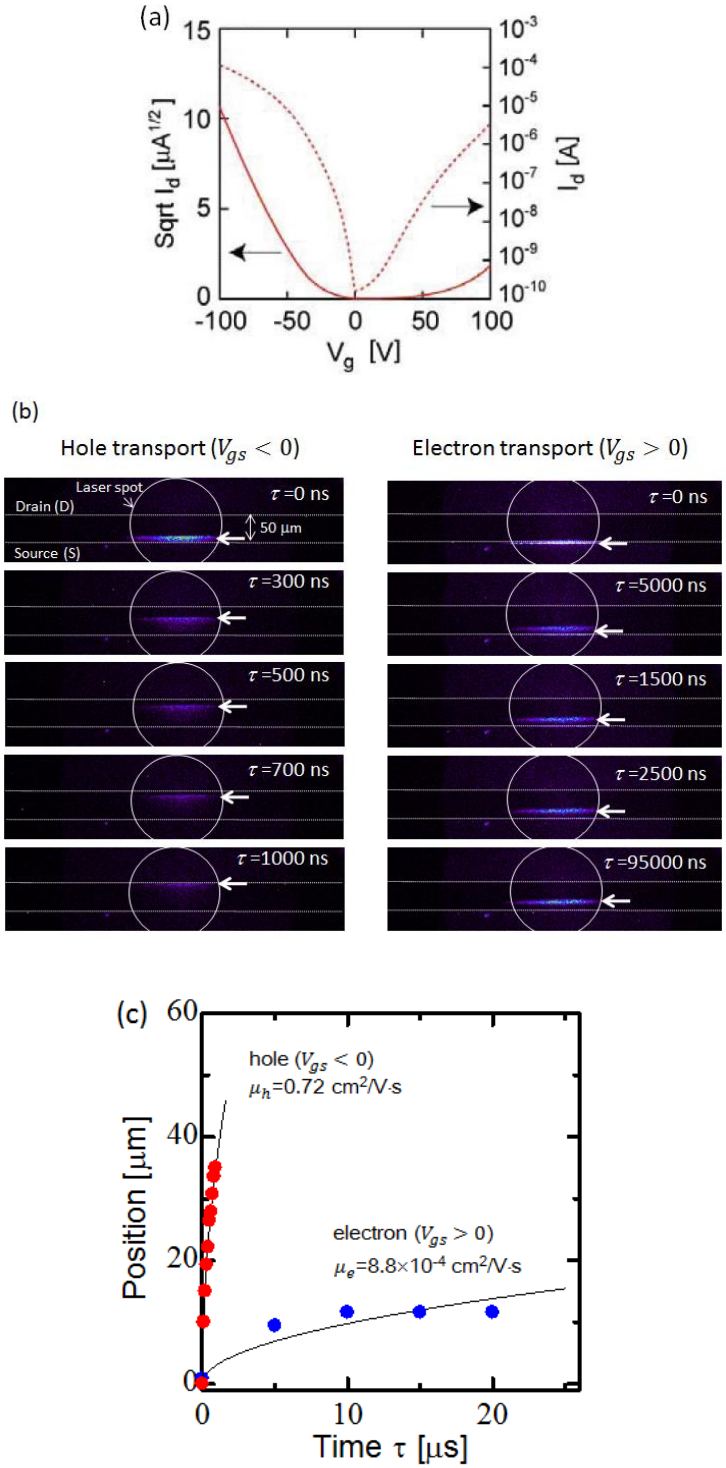

Figure 10: M. Iwamoto et al.

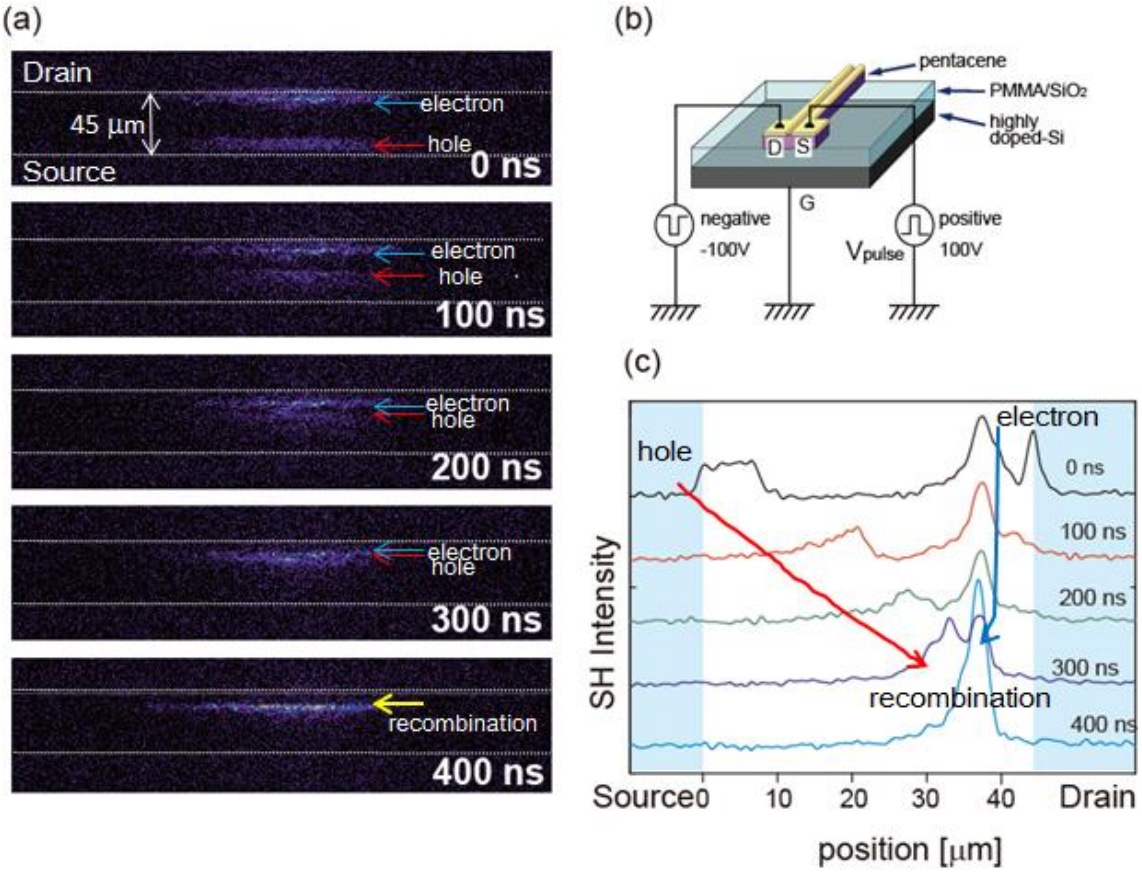

Figure 11: M. Iwamoto et al.

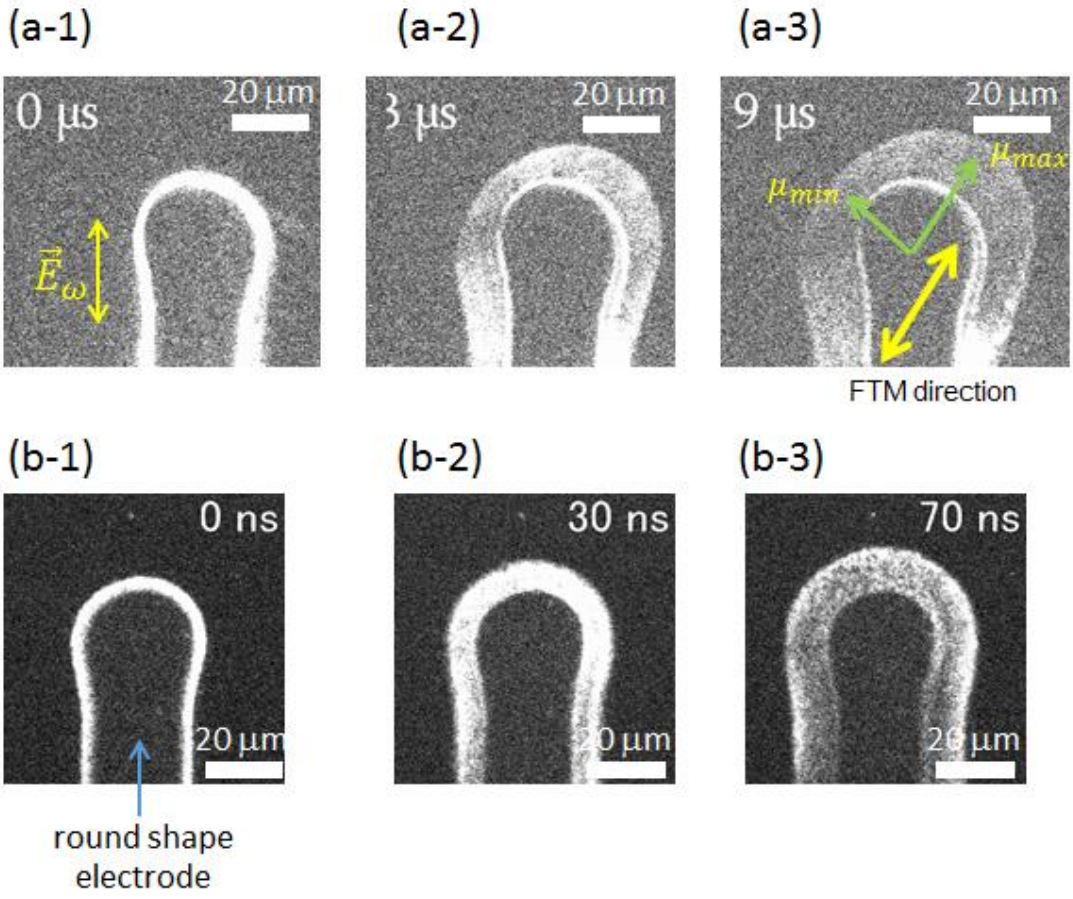

Figure 12: M. Iwamoto et al.

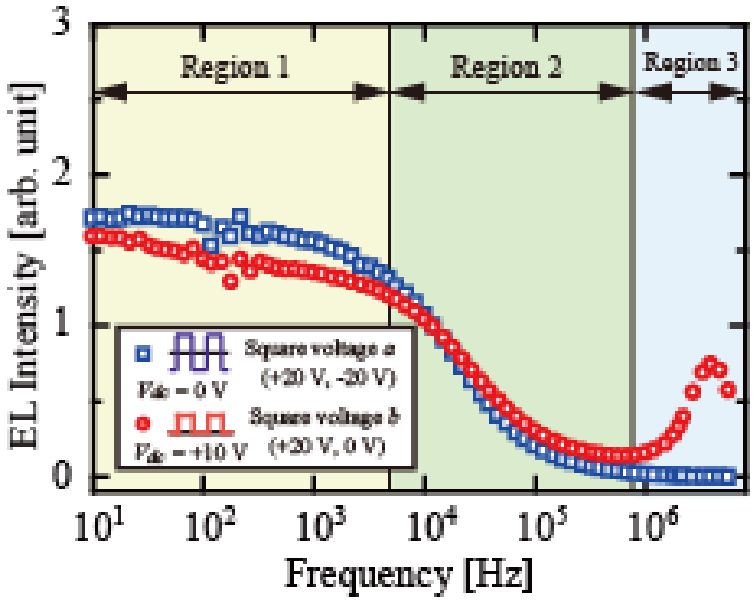

Figure 13: M. Iwamoto et al.

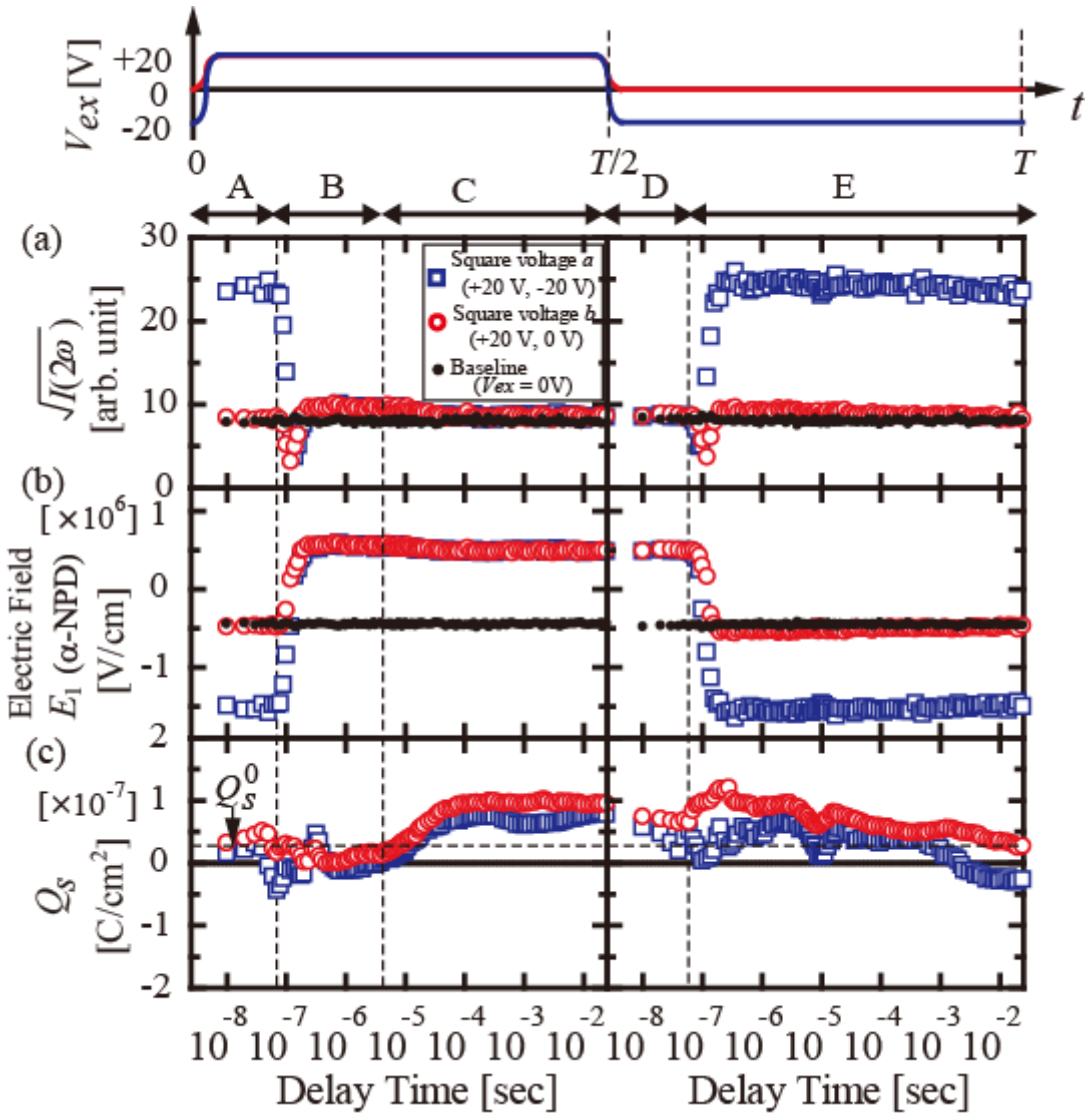

Figure 14: M. Iwamoto et al.

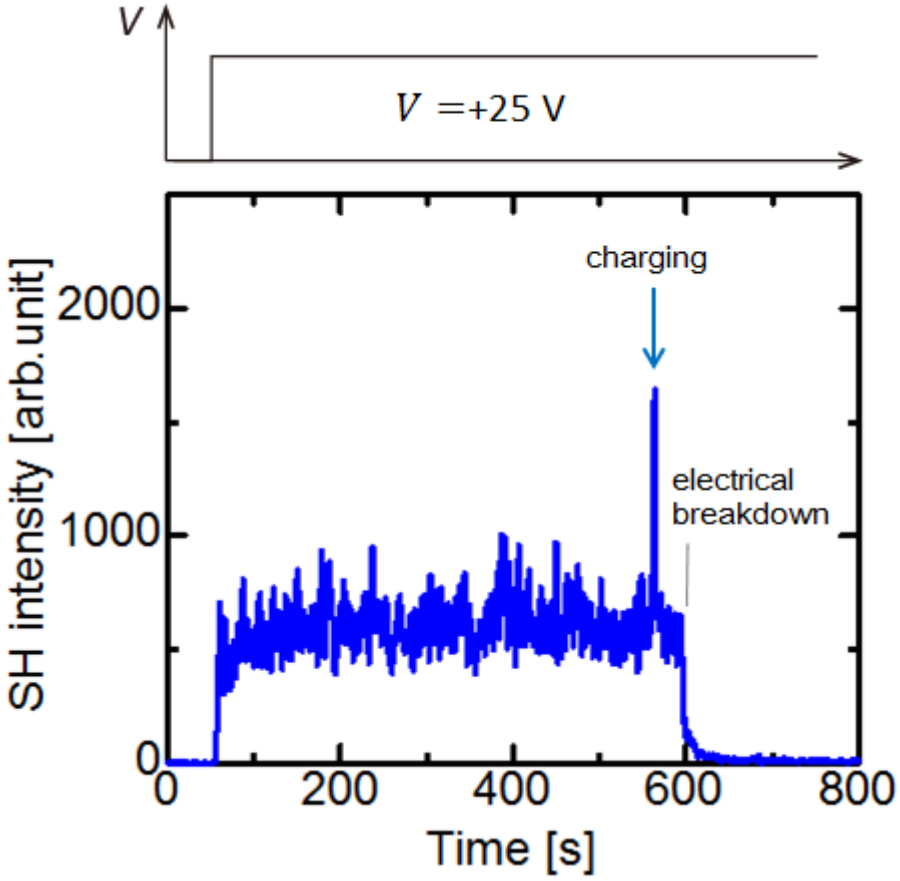

Figure 15: M. Iwamoto et al.

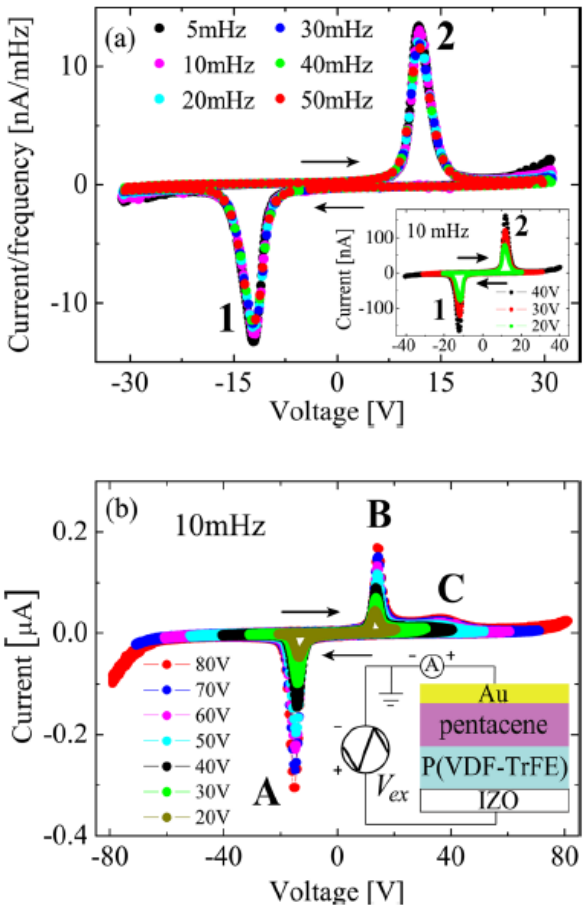

Figure 16: M. Iwamoto et al.

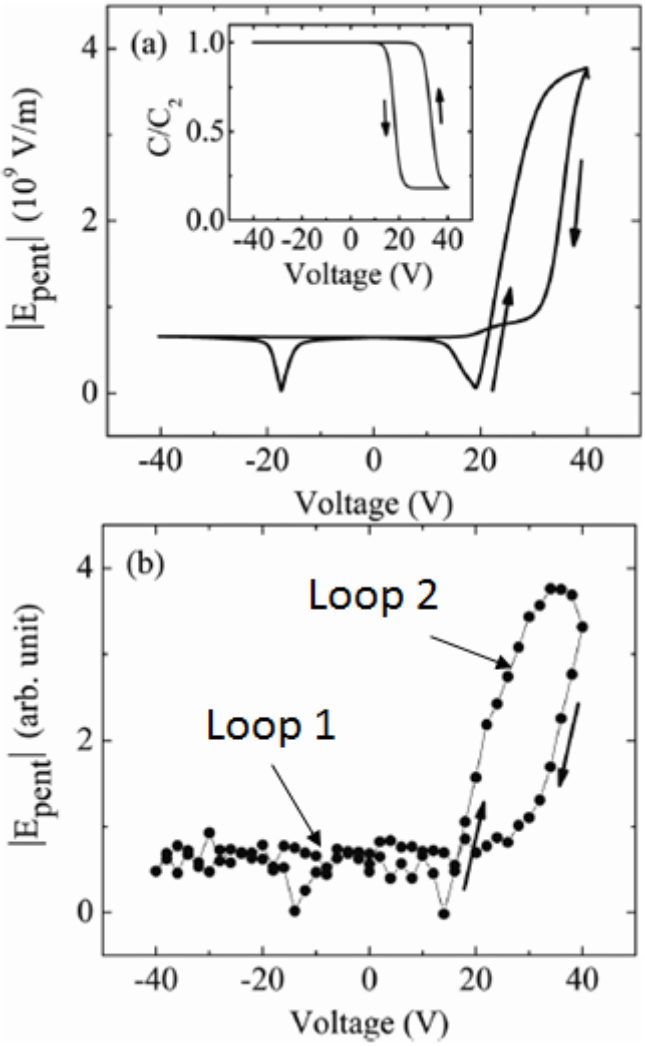

Figure 17: M. Iwamoto et al.